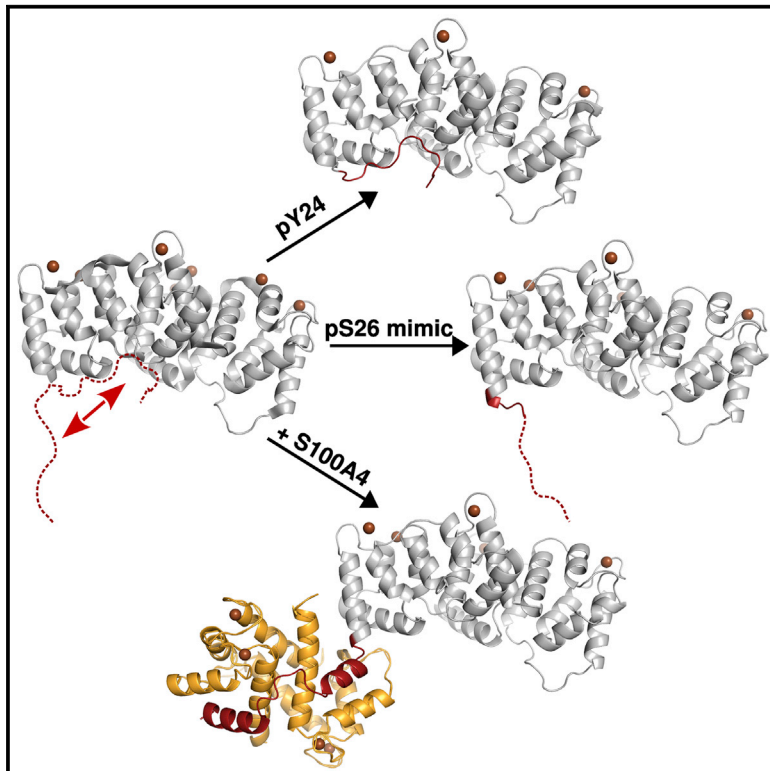


Structure

Regulation of the Equilibrium between Closed and Open Conformations of Annexin A2 by N-Terminal Phosphorylation and S100A4-Binding

Graphical Abstract



Authors

Péter Ecsédi, Bence Kiss, Gergő Gógl, ..., Gitta Schlosser, Gergely Katona, László Nyitray

Correspondence

nyitray@elte.hu

In Brief

Ecsédi et al. report the crystal structures of annexin A2 (ANXA2) phosphorylated at Tyr24, its phosphomimicking mutant S26E, and the ANXA2-S100A4 complex. Their work shed light on how the alterations in structure and dynamics of the N-terminal domain modulate ANXA2 function.

Highlights

- A short sequence motif within ANXA2 NTD is responsible for clamping the NTD to the CTD
- Phosphorylation of Tyr24 anchors the NTD to the core and inhibits membrane aggregation
- Upon Ser26 phosphorylation, the NTD is released from the CTD
- Asymmetric binding of S100A4 to the whole NTD promotes membrane crosslinking

Data Resources

5LPU
5LQ0
5LQ2
5LPX

Regulation of the Equilibrium between Closed and Open Conformations of Annexin A2 by N-Terminal Phosphorylation and S100A4-Binding

Péter Ecsédi,^{1,9} Bence Kiss,^{1,9} Gergő Gógl,¹ László Radnai,² László Buday,² Kitti Koprivanacz,² Károly Liliom,² Ibolya Leveles,^{2,3} Beáta Vértessy,^{2,3} Norbert Jeszenői,^{4,5} Csaba Hetényi,⁶ Gitta Schlosser,⁷ Gergely Katona,⁸ and László Nyitrai^{1,10,*}

¹Department of Biochemistry, ELTE Eötvös Loránd University, 1117 Budapest, Hungary

²Institute of Enzymology, Hungarian Academy of Sciences, 1117 Budapest, Hungary

³Department of Applied Biotechnology, Budapest University of Technology and Economics, 1117 Budapest, Hungary

⁴Department of Genetics, ELTE Eötvös Loránd University, 1117 Budapest, Hungary

⁵Institute of Physiology, University of Pécs, 7625 Pécs, Hungary

⁶Department of Pharmacology and Pharmacotherapy, University of Pécs, 7624 Pécs, Hungary

⁷MTA-ELTE Research Group of Peptide Chemistry, ELTE Eötvös Loránd University, 1117 Budapest, Hungary

⁸Department of Chemistry and Molecular Biology, University of Gothenburg, Gothenburg 40530, Sweden

⁹These authors contributed equally

¹⁰Lead Contact

*Correspondence: nyitrai@elte.hu

<http://dx.doi.org/10.1016/j.str.2017.06.001>

SUMMARY

Annexin A2 (ANXA2) has a versatile role in membrane-associated functions including membrane aggregation, endo- and exocytosis, and it is regulated by post-translational modifications and protein-protein interactions through the unstructured N-terminal domain (NTD). Our sequence analysis revealed a short motif responsible for clamping the NTD to the C-terminal core domain (CTD). Structural studies indicated that the flexibility of the NTD and CTD are interrelated and oppositely regulated by Tyr24 phosphorylation and Ser26Glu phosphomimicking mutation. The crystal structure of the ANXA2-S100A4 complex showed that asymmetric binding of S100A4 induces dislocation of the NTD from the CTD and, similar to the Ser26Glu mutation, unmasks the concave side of ANXA2. In contrast, pTyr24 anchors the NTD to the CTD and hampers the membrane-bridging function. This inhibition can be restored by S100A4 and S100A10 binding. Based on our results we provide a structural model for regulation of ANXA2-mediated membrane aggregation by NTD phosphorylation and S100 binding.

INTRODUCTION

Annexin A2 (ANXA2) is a member of the non-EF-hand Ca²⁺ binding protein family of annexins consisting of 12 paralogs in humans (Gerke and Moss, 2002). ANXA2 is characterized by the ability to bind and aggregate (“annex”) anionic phospholipid membranes in a calcium-dependent manner (Drust and Creutz, 1988). This ability underlies its biological functions including

vesicular transport, exocytosis, and endocytosis. Overexpression of ANXA2 is observed in various tumor types and it contributes to cancer development through affecting tumor cell adhesion, proliferation, apoptosis, invasion as well as tumor neovascularization (Xu et al., 2015).

Annexins consist of a disordered N-terminal domain (NTD, ANXA2 residues 2–33) (Figure 1A) followed by a conserved C-terminal core domain (CTD, ANXA2 residues 34–339) comprising four annexin repeats (Gerke and Moss, 2002). The convex side of CTD is responsible for calcium binding mediating the canonical membrane-binding properties of ANXAs. The concave surface, on the other hand, has a role in membrane bridging mediated by ANXA1, ANXA2, and ANXA4 paralogs in vertebrates. This side of annexins also anchors the C terminus of the NTD (C-NTD, ANXA2 residues 24–33). Although the NTD is relatively short compared with the CTD, its highly variable length and sequence underlies paralog-specific functions in the annexin family (Lizarbe et al., 2013). A unique structural feature of ANXA1 is that an amphipathic helix of the NTD is inserted into the annexin repeat III. Upon Ca²⁺ binding, this helix is rejected and the C-NTD also dissociates from the CTD. These structural changes are implicated in the ANXA1-induced membrane aggregation (Rosegarth and Luecke, 2003). In the case of ANXA2 and ANXA4, Ca²⁺ binding does not lead to a conformational rearrangement of the C-NTD (Rosegarth and Luecke, 2004; Seaton, 1996). On the other hand, Ser26 and Thr6 in ANXA2 and ANXA4, respectively, are located at structurally identical positions and both are prone to protein kinase C (PKC) phosphorylation (Gould et al., 1986; Weber et al., 1987). Note that ANXA1 comprises alanine in the homologous position. Based on the crystal structures of ANXA4 and its phosphomimicking Thr6Asp mutant, phosphorylation of Thr6 results in the dislocation of the NTD, which leads to impaired ANXA4-mediated membrane aggregation (Kaetzel et al., 2001). Regarding ANXA2, the mutually exclusive phosphorylation of Ser12 and Ser26 by PKC (Gould et al., 1986; He et al., 2011; Jost and Gerke, 1996) and Tyr24 by c-Src (Erikson and Erikson,

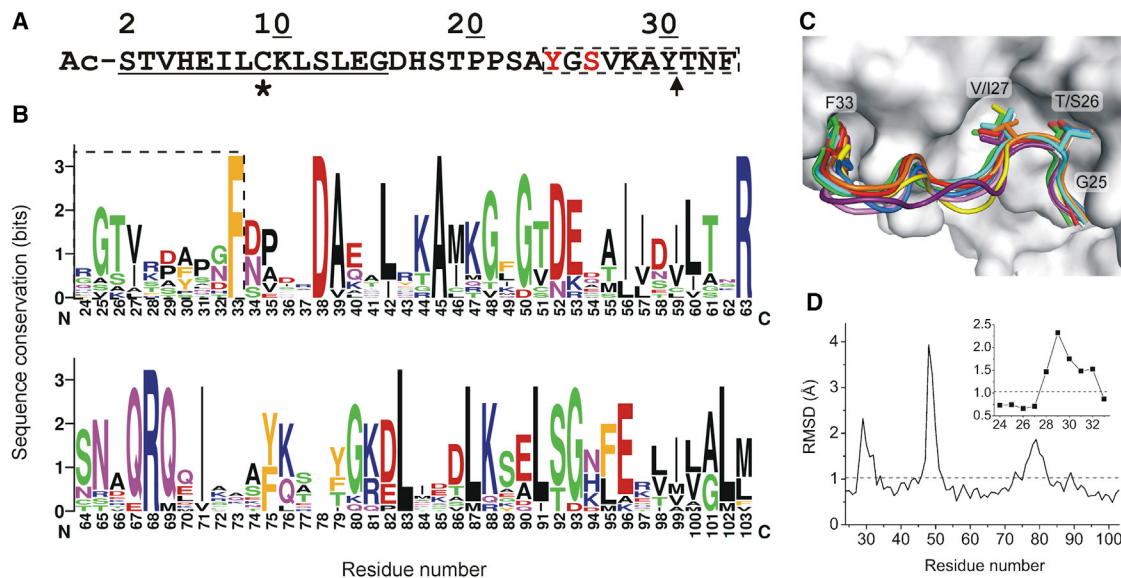


Figure 1. Sequence and Structure Alignment of Annexin C-NTDs

(A) Amino acid sequence of ANXA2 NTD. The S100A10 binding site is underlined. The asterisk indicates Cys9, which is conjugated with a fluorescein moiety in Fl-ANXA2 variants. The C-NTD is shown in a dashed box. Phosphorylatable Tyr24 and Ser26 are red, while the black arrow indicates the α -chymotrypsin cleavage site. Note that the initiator methionine is cleaved off and serine at position 2 is acetylated.

(B) LOGO representation of the sequence conservation within the C-NTD (highlighted with dashed lines) and annexin repeat I created from human ANXA1-11 and ANXA13 amino acid sequences (according to ANXA2 numbering). As ANXA6 consists of two annexin modules, 13 identical sequences were used.

(C) The crystal structures of pig ANXA1 (PDB: 1HM6, chains A and B are purple and pink, respectively), human ANXA3 (PDB: 1AXN, blue), human ANXA4 (PDB: 2ZOC, cyan), human ANXA5 (PDB: 1ANX, green), human ANXA6 N-terminal module (PDB1M9I, yellow), bovine ANXA6 C-terminal module (PDB: 1AVC, orange), and hydra ANXB12 (PDB: 1AEL, red) were superimposed on the structure of human ANXA2 (PDB: 1XJL, white).

(D) RMSD was calculated for C α atoms using ANXA2 atomic positions as the reference. The dashed line indicates the mean RMSD value of region 24–103. The inset shows the RMSD of residues 24–33 corresponding to the C-NTD.

1980) negatively regulates the ANXA2-dependent membrane aggregation (Ayala-Sanmartin et al., 2000; Hubaishy et al., 1995; Johnstone et al., 1992). However, no structural data for the phosphorylated ANXA2 is available.

In addition to Ca²⁺ binding and protein phosphorylation, the function of ANXA1 and ANXA2, which have relatively long NTDs, is regulated by the binding of S100 proteins (Eden et al., 2016; Liu et al., 2015; Poeter et al., 2013). S100 proteins are small, dimeric EF-hand Ca²⁺ binding proteins that are expressed exclusively in vertebrates. In the presence of Ca²⁺, a hydrophobic interaction surface, which is buried in the apo form, is exposed (Bresnick et al., 2015). S100A10 represents an exception in the family, because it is unable to bind Ca²⁺ and adopts a constitutively active open conformation. S100A10 has been described as p11 in a symmetric complex with p36 (ANXA2) forming calpactin I (Gerke and Weber, 1984; Glenney and Tack, 1985). Later it has been demonstrated that other members of the S100 family (S100A4, S100A6, and S100A11) also interact with ANXA2 (Liu et al., 2015); however, structural data are available only for the ANXA2-S100A10 complex (Dempsey et al., 2012; Oh et al., 2013; Rety et al., 1999). The impact of S100A10 binding on the membrane-bridging function of ANXA2 has been widely investigated in terms of intracellular membrane fusions, such as chromaffin granule exocytosis (Chasserot-Golaz et al., 1996; Drust and Creutz, 1988). In addition, ANXA2 (alone or in complex with S100A10) has been implicated in cell-cell interactions, such as phagocytosis of apoptotic cells

(Fang et al., 2012), tight junction assembly (Lee et al., 2004), and tumor cell adhesion to endothelial cells (Tressler et al., 1993).

The regulation of ANXA2 function is highly complex: it involves Ca²⁺ binding, protein phosphorylation and the interaction with S100 proteins, and it also depends on experimental conditions, such as pH and membrane lipid composition. Several different topological models have been proposed to explain ANXA2-mediated membrane aggregation (Ayala-Sanmartin et al., 2008; Drucker et al., 2013; Illien et al., 2010; Liu, 1999); however, without knowledge of any 3D structures for phosphorylated ANXA2, the mechanism of phosphorylation-mediated regulation remained unclear.

In this study we investigated the consequences of C-NTD phosphorylation and S100 binding on ANXA2 structure by X-ray crystallography, molecular dynamics (MD) simulations, thermal unfolding, and limited proteolysis assays. We also studied the effect of S100 binding and/or protein phosphorylation on ANXA2-mediated liposome aggregation. We found that Tyr24 phosphorylation reduced the conformational fluctuation of the C-NTD and it hampers the ability of ANXA2 to aggregate phosphatidylserine-containing large unilamellar vesicles (LUVs). However, the addition of S100A4 or S100A10 restored ANXA2 activity. In contrast, the phosphomimicking Ser26Glu mutation substantially increased the conformational freedom of the C-NTD and did not interfere with the membrane crosslinking activity of ANXA2. 3D structure determination and analysis of the ANXA2-S100A4 complex revealed that the entire NTD of

ANXA2 is wrapped around an S100A4 dimer forming an asymmetric complex, which resembles the interaction of S100A4 with non-muscle myosin IIA (NMIIA). Based on our results, we provide a plausible model for the regulation of ANXA2-mediated membrane aggregation by C-NTD phosphorylation or S100 binding.

RESULTS

Sequence and Structure Conservation in the NTD of Annexins

Although the sequence conservation in annexin NTD is markedly lower than in the CTD, the alignment of human annexin sequences revealed a short sequence motif G-[TS]-[VI] (residues 25–27 in ANXA2) in the C-NTD (Figure 1B). To investigate the structural aspects of this sequence conservation, the 3D structures of wild-type annexins were aligned (Figure 1C), followed by the calculation of the root-mean-square deviation (RMSD) values for C α atoms. We found that G-[TS]-[VI] motif can be characterized by a markedly lower conformational flexibility than the subsequent part of the C-NTD, being one of the structurally most conserved regions of annexins (Figure 1D). Here the side chain of Val/Ile27 fits into a hydrophobic pocket formed by annexin repeats I and IV. The hydroxyl group of the Thr26 side chain faces inward and forms hydrogen bonds with the carbonyl oxygens of Ser296 and Val334, while the outward-pointing methyl group makes van der Waals contact with the solvent-accessible side chain of Leu301 in annexin repeat IV (Aukrust et al., 2006). Note that in annexins A1, A8, and A13, which do not comprise the regular G-[TS]-[VI] motif, the hydrophobic residue at position 301 is replaced by Asn or Gln. Finally, Gly25 enables Thr/Ser26 and Val/Ile27 to adopt an optimal conformation for binding to CTD without undue strain. Based on these observations, we suggest that the G-T/S-V/I motif is responsible for clamping the C-NTD to the CTD in a strictly defined conformation. Furthermore, this high sequence and structure conservation also suggests that the phosphorylation state of Ser26, similar to the phosphorylation of Thr6 in ANXA4 (Kaetzel et al., 2001), could play an important role in the modulation of ANXA2 structure.

Effect of the C-NTD Phosphorylation on ANXA2 Structure

To shed light on the regulatory mechanism driven by ANXA2 phosphorylation, we conducted structural studies using phosphorylated and phosphomimetic ANXA2 variants. Selective phosphorylation of Tyr24 could be achieved using ephrin-B1 kinase domain expressed in *E. coli* in an active form, while a Ser-to-Glu mutation was introduced into ANXA2 for mimicking, to a certain extent, Ser26 phosphorylation. Both variants were successfully crystallized in the presence of Ca²⁺, and the 3D structures were solved by molecular replacement to 2.9 and 3.4 Å resolutions for ANXA2^{pY24}, and to 1.9 Å resolution for ANXA2^{S26E} (Table 1). Both ANXA2^{pY24} structures revealed that the conformation of the C-NTD is identical to the native state, but a salt bridge is formed between the C-NTD and CTD by the pTyr24 and Lys302 side chains (Figure 2A). Moreover, the 3.4 Å resolution structure (PDB: 5LQ2) was isomorphous to the crystal structure of the Ca²⁺-bound full-length ANXA2 (PDB: 1XJL), allowing direct comparison of their temperature factors. In the case of native ANXA2, the average B factor of

the C-NTD was 62% higher than that of the overall structure, the value of which was reduced to 29% upon Tyr24 phosphorylation (Figure 2A). To further investigate this finding, 300 ns long MD simulations were carried out using the crystal structure of the Ca²⁺-bound ANXA2 (PDB: 1XJL). The “core” structure (residues 21–339) was identical in the ANXA2 and ANXA2^{pY24} simulations to minimize model bias. MD simulations supported the idea that pTyr24 acts as an anchor to clamp the C-NTD to the CTD through an ionic interaction with Lys302. Root-mean-square fluctuation (RMSF) analysis showed that, in ANXA2^{pY24}, the amino acid region 10–24 was markedly less flexible than the corresponding region in the unphosphorylated ANXA2 (Figure 2B).

In contrast to ANXA2 and ANXA2^{pY24} structures, the C-NTD is almost completely invisible in the crystal structure of ANXA2^{S26E} (Figure 2A), resembling the 3D structure of ANXA4^{T6D} (Kaetzel et al., 2001). Here the cavity in annexin repeat I, which originally accommodates the side chain of the conserved Phe33, is occupied by that of Tyr30 (Figure 2A). To carry out MD simulation of ANXA2^{pS26} using the crystal structure 1XJL as initial state, the main chain conformation of the C-NTD had to be altered in order to resolve atomic clashes that appeared upon in silico phosphorylation of Ser26 (Figure S1A). This modification led to the dissociation of the conserved interactions formed by Ser26 and Val27 side chains with the CTD. Although a novel ionic interaction was formed between the pSer26 and Arg304 side chains, it seemed to be rather transient during the 300 ns long MD simulation (Figure S1B). To overcome the bias potentially caused by the manipulation of the highly conserved C-NTD conformation, the MD simulation was also performed using the ANXA2^{S26E} crystal structure as initial state. Here, the RMSF values not only of the NTD, but also the CTD, are significantly higher in ANXA2^{pS26} than in the unphosphorylated ANXA2 (Figure 2B). The pSer26 side chain has a tendency to form ionic interactions with the basic residues Lys28, Arg37, and Arg63, which is presumably initiated by the swapping of Phe33 for Tyr30 (Figure 2A). However, the relatively high RMSF value of pSer26 indicates that these interactions are rather transient, which could explain why the residues N-terminally located from Ala29 are invisible in the crystal structure. To illustrate the effect of the NTD phosphorylation on ANXA2 flexibility in a more expressive way, frames were collected from the MD simulations every 3 ns and aligned (Figure 2C). Here the “fuzziness” of ANXA2^{S26E} structure is markedly higher than that of ANXA2, while the ANXA2^{pY24} structure shows the lowest fluctuation suggesting that the phosphorylation events affect the conformational flexibility not only of the NTD, but also of the CTD.

C-NTD Phosphorylation Modulates ANXA2 Stability

To investigate experimentally the effects of Tyr24 phosphorylation and Ser26Glu mutation on structural dynamics and stability in solution, we used limited proteolysis (LP) and differential scanning fluorimetry (DSF) assays, respectively (Figures 2D–2F and Table S1). It was previously demonstrated that full-length ANXA2 could be cleaved between Tyr30 and Thr31 by α -chymotrypsin, and the proteolysis was readily followed using ANXA2 labeled at Cys9 with the fluorescent dye acrylodan (Johnsson et al., 1988). To assess the flexibility of the NTD, we used 5-IAF labeling at Cys9 (FI-ANXA2). LP assays confirmed the results presented above, since the cleavage of the NTD from

Table 1. X-Ray Crystallography Data Collection and Refinement Statistics

	ANXA2 ^{S26E} (5LPX)	ANXA2 ^{pTyr24} (5LQ0)	ANXA2 ^{pTyr24} (5LQ2)	ANXA2-S100A4 (5LPU)
Data Collection				
Space group	P2 ₁ 2 ₁ 2 ₁	P 2 ₁ 2 ₁ 2 ₁	P 2 ₁ 2 ₁ 2 ₁	P 1 2 ₁ 1
Cell dimensions				
<i>a</i> , <i>b</i> , <i>c</i> (Å)	54.95, 58.76, 182.09	56.45, 63.47, 268.91	61.37, 99.2, 173.02	71.74, 61.24, 148.16
α , β , γ (°)	90, 90, 90	90, 90, 90	90, 90, 90	90, 88.69, 90
Resolution (Å)*	47.05–1.9 (1.96–1.9)	47.77–2.9 (3.00–2.9)	86.51–3.4 (3.52–3.4)	49.37–2.1 (2.17–2.1)
<i>R</i> _{meas} (%)*	11.7 (156.1)	10 (62)	9.3 (63.8)	7 (120.5)
<i>I</i> / <i>σI</i> *	19.05 (2.30)	18.63 (3.22)	15.76 (2.91)	23.10 (2.42)
Completeness (%)*	99.99 (99.98)	99.12 (99.86)	99.23 (99.86)	99.98 (99.87)
Redundancy*	13.18 (9.34)	9.14 (6.33)	4.9 (3.84)	13.67 (9.95)
CC1/2*	99.9 (80.8)	99.9 (88.9)	99.9 (81.6)	100 (89.1)
Refinement				
Resolution (Å)	47.05–1.9	47.77–2.9	86.51–3.4	49.37–2.1
No. of reflections*	625,302 (43,675)	202,235 (13,862)	73,652 (5,641)	1,031,323 (74,556)
<i>R</i> _{work} / <i>R</i> _{free}	0.1467/0.182	0.2287/0.259	0.2036/0.238	0.182/0.207
No. of residues				
Protein	311	631	638	863
Glycerol	2	0	0	5
Ca ²⁺	5	6	10	14
Water	480	7	2	288
B factors				
Protein	32.59	64.37	93.52	76.27
Water	47.9	37.67	65.88	59.88
RMSD				
Bond lengths (Å)	0.019	0.003	0.011	0.004
Bond angles (°)	1.47	0.67	1.43	0.75
Ramachandran (%)				
Favored	98	97	89	97
Outliers	0.32	0.32	0.63	0.23

Data were collected on single crystals. *Values for the highest-resolution shell are shown in parentheses. RMSD, root-mean-square deviation.

CTD by α -chymotrypsin was 2.1-times slower in the case of FI-ANXA2^{pY24} (Figure 2E; Table S1) than in the unphosphorylated FI-ANXA2. In turn, the susceptibility of FI-ANXA2^{S26E} to α -chymotrypsin digestion showed a 2.6-fold increase compared with FI-ANXA2. DSF experiments further corroborated the 3D structural data. Regardless of the presence of calcium ions, Tyr24 phosphorylation resulted in an increased thermal stability of ANXA2, while the phosphomimetic mutant ANXA2^{S26E} was characterized by decreased stability (Figure 2F; Table S1), in accordance with previous results performed by circular dichroism spectroscopy (Grindheim et al., 2014). Based on our crystal structures, MD simulations, and LP and DSF experiments we can conclude that the flexibility of the C-NTD and the stability of the CTD are clearly interrelated and oppositely regulated by Tyr24 phosphorylation and Ser26Glu phosphomimicking mutation.

Interaction of S100A4 and S100A10 with ANXA2 Variants in Solution

One of the most extensively characterized properties of ANXA2 is its interaction with S100A10 forming a heterotetrameric complex (calpactin I). However, it was demonstrated that S100A4

also binds to ANXA2 resulting in accelerated plasmin formation, and inducing angiogenesis in primary human endothelial cells. Furthermore, it was shown that S100A4 binding requires the entire NTD (Semov et al., 2005). To evaluate quantitatively the interaction of S100A4 with ANXA2, we performed fluorescence polarization (FP) binding studies using FI-ANXA2^{2–15} and FI-ANXA2^{2–33} fragments, as well as full-length FI-ANXA2 variants. Firstly, we determined the effect of the length of FI-ANXA2 constructs on S100 binding. As expected, S100A10 bound tightly to both NTD fragments, as well as all ANXA2 constructs, with a *K*_d of 10–40 nM (Figure 3A; Table S2). In contrast, the interaction of S100A4 with FI-ANXA2^{2–15} was very weak (*K*_d ≈ 60 μM). FI-ANXA2^{2–33}, representing the entire NTD, and the full-length FI-ANXA2 bound to S100A4 with one order of magnitude higher affinity (*K*_d = 2.4 and 5.0 μM, respectively) (Figure 3B and Table S2). (We should note here that the *K*_d values presented in the text and in Table S2 for S100A4 interaction with full-length NTD and ANXA2 variants were calculated based on the fact the a single NTD binds to an S100A4 dimer, forming an asymmetric complex; see below.) Then we evaluated the effect of the C-NTD phosphorylation on the ANXA2-S100

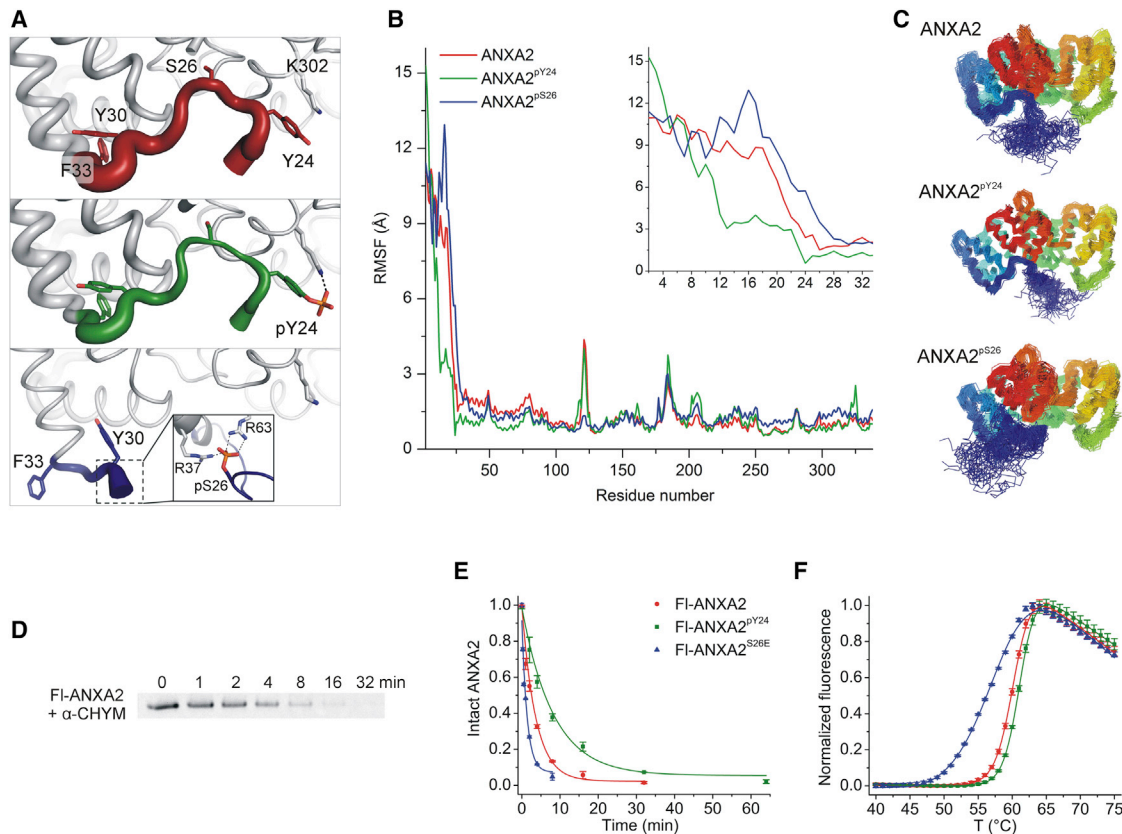


Figure 2. Structural and Dynamic Changes in ANXA2 upon Phosphorylation

(A) Putty representation of native ANXA2 (PDB: 1XJL, chain A), ANXA2^{PY24} (PDB: 5LQ2, chain B), and ANXA2^{S26E} (PDB: 5LPX) highlighting the C-NTD with red, green, and blue, respectively. Transient ionic interactions of pSer26 during the MD simulation of ANXA2^{S26E} (using the crystal structure 5LPX as initial state) are depicted in the inset. Note that, for B factor putty representation, the equivalent chains in the crystal lattice were used.

(B) Root-mean-square fluctuation (RMSF) per residue ($C\alpha$) of ANXA2 variants during the 300 ns long MD simulations.

(C) Frames were extracted from the simulations every 3 ns and aligned for visualizing alternatively the effect of phosphorylation events on the overall structure of ANXA2.

(D) Flexibility of ANXA2 NTD was followed by chymotryptic cleavage of fluorescently labeled ANXA2 variants. Samples were separated on Tris-Tricine-SDS gels, and intact ANXA2 bands were visualized using blue-light transillumination.

(E) Densitometric analysis of intensity values were normalized and plotted against time. Data points represent the mean \pm SEM of two independent experiments. Solid line indicates a single exponential fit to the data.

(F) Thermal stability of the unlabeled ANXA2 variants were investigated in differential scanning fluorimetry experiments. Data points represent the mean \pm SEM of three independent experiments. Solid line indicates the data fitting according to the Gibbs-Helmholtz equation. See also Figure S1 and Table S1.

interactions. Since the S100A10 binding site is located in the N-terminal half of the NTD, it was not surprising that the affinity of FI-ANXA2^{PY24} and FI-ANXA2^{S26E} did not notably differ from that of FI-ANXA2. In contrast, S100A4 binding was affected by both Tyr24 phosphorylation and the phosphomimetic mutation of Ser26. As expected, FI-ANXA2^{PY24}, where the C-NTD is anchored to the CTD, showed reduced affinity to S100A4 ($K_d = 10.3 \mu\text{M}$) (Figure 3C), whereas FI-ANXA2^{S26E}, the variant that was characterized by having a released NTD, interacted with S100A4 as strong as FI-ANXA2²⁻³³ ($K_d = 2.2 \mu\text{M}$). Note that the corresponding relative binding strength (ANXA2^{S26E}:ANXA2:ANXA2^{PY24} = 2.1:1:0.44) nicely correlates with the relative susceptibility of the NTD to α -chymotrypsin digestion (2.6:1:0.5) of the same variants. To extend our studies beyond the structurally rigid ANXA2 “core,” we investigated the interaction of FI-ANXA2^{S12E-S26E} double mutant (mimicking the ANXA2 double-phosphorylated state) with S100 proteins. The introduc-

tion of the Ser12Glu mutation into the ANXA2^{S26E} variant caused a 20-fold drop in the binding affinity of S100A10 (Figure 3A and Table S2). By comparison, the Ser12Asp substitution in ANXA2²⁻¹⁵ was accompanied by a 13-fold affinity decrease (Becker et al., 1990). On the contrary, the S100A4-binding capability of ANXA2^{S26E} was not affected by the additional Ser-to-Glu substitution (Table S2).

Since we showed that S100A4 binds to ANXA2 forming a more extended interaction surface comprising about 30 residues, we hypothesized that ANXA2 binds to S100A4 in an asymmetrical manner similar to the S100A4-NMIIA and S100B-RSK1 interactions (Elliott et al., 2012; Gogl et al., 2016; Kiss et al., 2012). To address this question, we repeated the binding assays using 10 μM of FI-ANXA2²⁻³³ and FI-ANXA2. The data analysis was performed using the quadratic binding equation by fixing the previously measured K_d values. The resulting fluorescent reporter concentrations of 21.9 and 21.7 μM (instead of 8.8 and

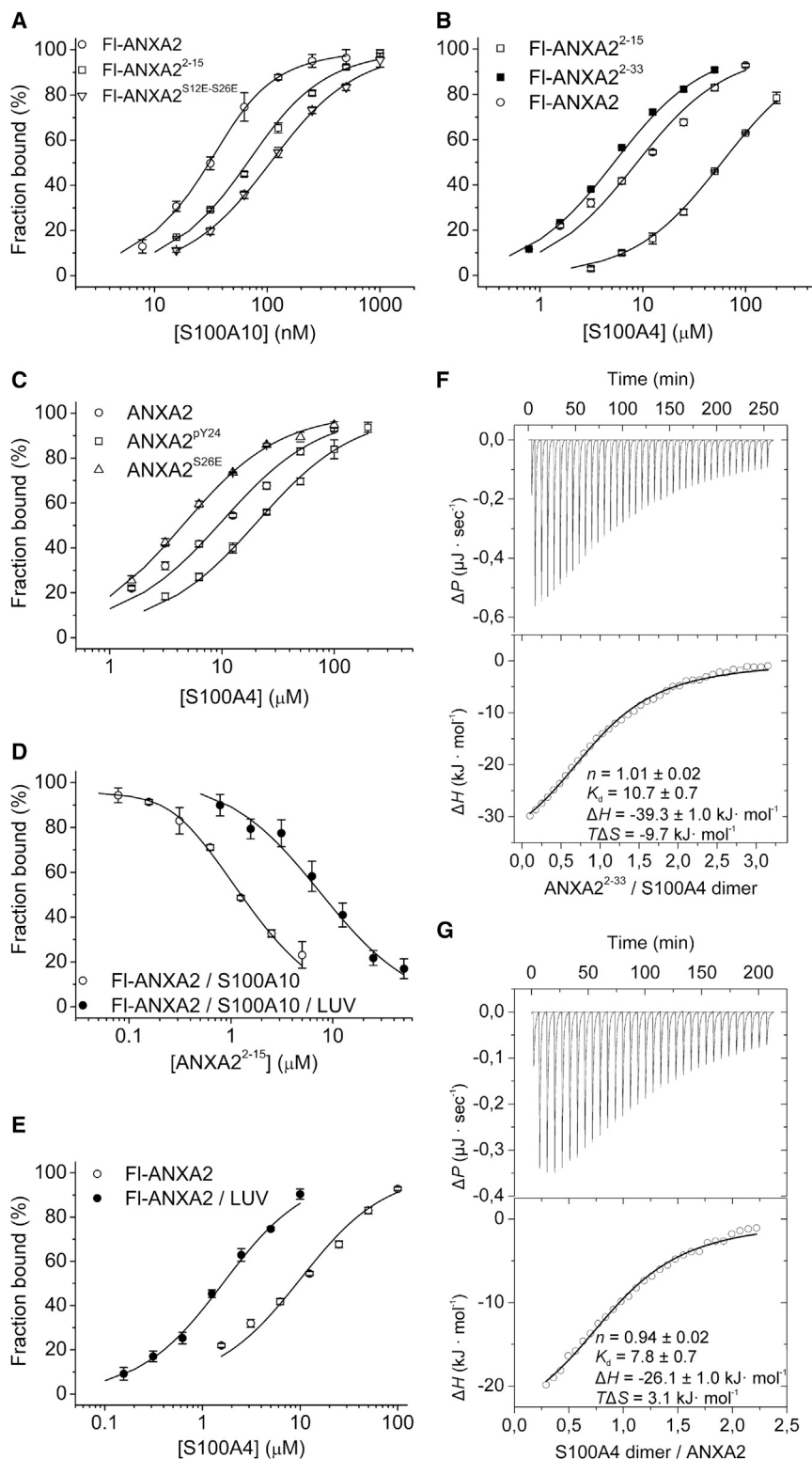


Figure 3. Interaction of S100A4 and S100A10 with ANXA2

(A to C) 50 nM FI-ANXA2 variants were titrated with S100A10 and S100A4 (monomeric S100 concentrations are shown). Complex formation was detected by an increase in the fluorescence polarization of the fluorescein moiety attached to Cys9. Each data point represents the mean \pm SEM of three independent experiments. Solid lines indicate the data fitting to quadratic binding equation. (D) 50 nM FI-ANXA2 / 250 nM S100A10 was titrated with unlabeled ANXA2²⁻¹⁵ peptide in the presence or in the absence of 100 μM LUVs. Solid lines show the data fitting to a competitive binding equation. (E) 50 nM FI-ANXA2 was titrated with S100A4 (monomeric concentration) in the absence or in the presence of 50 μM LUVs (PC:PS:Chol, 40:20:40). Solid lines show the data fitting to a quadratic binding equation. All experiments were carried out in the presence of 2 mM CaCl₂. See Table S2 for more information.

(F and G) In an isothermal titration calorimeter 50 nM FI-ANXA2 / 250 nM S100A10 was titrated with unlabeled ANXA2²⁻¹⁵ peptide in the presence or in the absence of 100 μM LUVs. Solid lines show the data fitting to a competitive binding equation.

label-free isothermal titration calorimetry measurements confirmed that S100A4 binds to ANXA2 with moderate affinity ($K_d \approx 11$ and 8 μM for the NTD and full-length ANXA2, respectively) and with a stoichiometry of one ANXA2 chain to an S100A4 dimer (Figures 3F and 3G).

Interaction of S100A4 and S100A10 with Membrane-Bound ANXA2

To investigate the potential effect of ANXA2 membrane binding on its interaction with S100 proteins, we repeated the FP binding studies with the addition of LUVs containing phosphatidylcholine, phosphatidylserine, and cholesterol in a molar ratio of 40:20:40, respectively (Ayala-Sanmartin et al., 2001). Both S100 proteins bound to FI-ANXA2 variants with a significantly increased affinity. In the case of S100A10, the stoichiometry of the interaction was 1:1. As we had to apply 50 nM FI-ANXA2 reporters in the binding assays to yield a satisfying signal-to-noise ratio, only the upper limit of the K_d values could be determined, which were in the nanomolar range, with the exception of ANXA2^{S12E-S26E} ($K_d \approx 20$ nM). Therefore, we carried out competitive

titrations using ANXA2²⁻¹⁵ peptide as a competitor, which showed that, in the presence of LUVs, S100A10 bound to ANXA2 variants 4.4- to 7-fold stronger than in the absence of the vesicles (Figure 3D; Table S2). A similar increase in affinity was

titrations using ANXA2²⁻¹⁵ peptide as a competitor, which showed that, in the presence of LUVs, S100A10 bound to ANXA2 variants 4.4- to 7-fold stronger than in the absence of the vesicles (Figure 3D; Table S2). A similar increase in affinity was

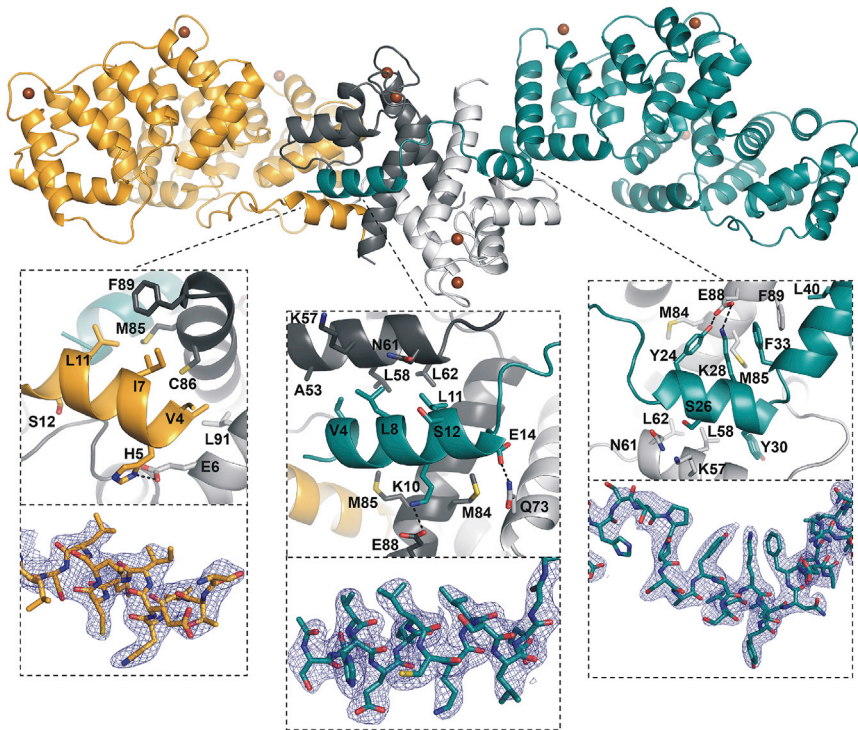


Figure 4. Crystal Structure of the ANXA2-S100A4 Complex

The interaction of ANXA2-A (bright orange) with S100A4-C (dark gray) is predominated by hydrophobic contacts (left panel) resembling the ANXA2-S100A10 complex (PDB: 4HRE). In contrast, the NTD of ANXA2-B (teal) is wrapped around the two S100A4 subunits, forming an asymmetric complex. Amino acid regions 2–14 (middle panel) and 23–31 (right panel) adopt an α -helical conformation and bind to S100A4-C (dark gray) and S100A4-D (light gray) subunits, respectively, with a nearly identical topology. Furthermore, the Phe89 side chain of S100A4-D is stacked between the hydrophobic side chains of Phe33 and Leu40 in ANXA2-B core domain (right panel). Calcium ions are shown as brown spheres.

ANXA2-B the entire NTD is wrapped around the S100A4 dimer resembling the asymmetrical complex of S100A4 with NMIIA (Kiss et al., 2012). Here, not only residues 2–14, but also the region 23–31 adopts an α -helical conformation, the helices of which bind to the “canonical” binding groove of each S100A4 subunit in a nearly identical manner. The

measured with S100A4, which interacted with LUV-bound FI-ANXA2, FI-ANXA2^{pY24}, and FI-ANXA2^{S26E} with K_d values of 0.8, 1.3, and 0.4 μ M, respectively (Figure 3E and Table S2). Note that the relative binding strength of the three FI-ANXA2 variants (ANXA2^{S26E}:ANXA2:ANXA2^{pY24} = 1.6:1:0.5) resemble those of in the absence of LUVs (2.1:1:0.44). In this respect, ANXA2^{S12E–S26E} behaved anomalously, since only a 1.8-fold LUV-dependent affinity increase was measured (Table S2). To determine the stoichiometry of the interaction of membrane-bound ANXA2 with S100 proteins, we repeated the binding studies with 1.5 μ M FI-ANXA2/1 mM LUVs. In the case of S100A4, the data analysis (by fixing the K_d to 1.6 μ M) resulted in a fluorescent reporter concentration of 3.5 μ M, which supports that S100A4 binds to ANXA2 asymmetrically in its membrane-bound form as well (Table S2).

Crystal Structure of the ANXA2-S100A4 Complex

The crystal structure of S100A10 complexed with ANXA2^{2–14} peptide (PDB: 1BT6) or the full-length ANXA2 (PDB: 4HRE) showed that two ANXA2 chains bind symmetrically to the dimeric S100A10 protein. Here, we report the 2.1 Å crystal structure of the ANXA2-S100A4 complex, where we observed also a heterotetrameric complex in the asymmetrical unit with five Ca²⁺ bound by each annexin chain and four Ca²⁺ bound by the S100A4 dimer (Figure 4). Strikingly, the two ANXA2 chains (referred to as ANXA2-A and ANXA2-B) bind to S100A4 in a profoundly different way. The binding mode of segment 2–14 of ANXA2-A is identical to that seen in the crystal structure of ANXA2-S100A10 complexes. However, the N-terminal acetyl group could not be modeled as the extreme N terminus of ANXA2-A is rather solvent accessible and does not contact the first helix of S100A4-C (the two chains of S100A4 are denoted as S100A4-C and S100A4-D). On the contrary, in the case of

intervening proline-rich region (residues 15–22) acts as a loosely bound bridge between the two anchoring helices. The N-terminal helix forms mainly hydrophobic contacts, while the C-terminal helix forms both hydrophobic and polar interactions with S100A4. The complex is further stabilized by hydrophobic contacts between S100A4 and the CTD of ANXA2, as the side chain of Phe89-D is stacked between the side chains of Phe33-B and Leu40-B. The hydroxyl group of the phosphorylatable Tyr24-B, as well as the ϵ -amino group of the Lys28-B, is the part of a hydrogen-bonding network connected by the Glu88-D carboxyl group. The phosphorylatable Ser26-B side chain makes van der Waals contact with Lys57-D and Asn61-D, while the Ser12-B side chain points outward explaining the neutral effect of Ser12-Glu substitution on the ANXA2-S100A4 interaction (Figure 4). Based on the crystal structure, one could assume that both phosphorylation events in the C-NTD interfere with S100A4 binding. While Tyr24 phosphorylation would result in a repulsive electrostatic interaction between pTyr24-B and Glu88-D and cause atomic clashes, Ser26 phosphorylation or Ser26Glu substitution could be sterically unfavorable. However, the experimental findings, which show that the affinity of S100A4 to the different ANXA2 variants is well correlated with the differences measured in the NTD conformational flexibility, support the hypothesis that the phosphorylation events regulate the complex formation between ANXA2 and S100A4 indirectly.

Regulation of ANXA2-Mediated LUV Bridging by Phosphorylation and S100 Binding

To evaluate the functional role of the NTD-related processes, we investigated ANXA2-mediated liposome aggregation. Firstly, we determined the LUV-bridging capability of the different ANXA2 variants comprising the NTD, as well as a deletion mutant of ANXA2

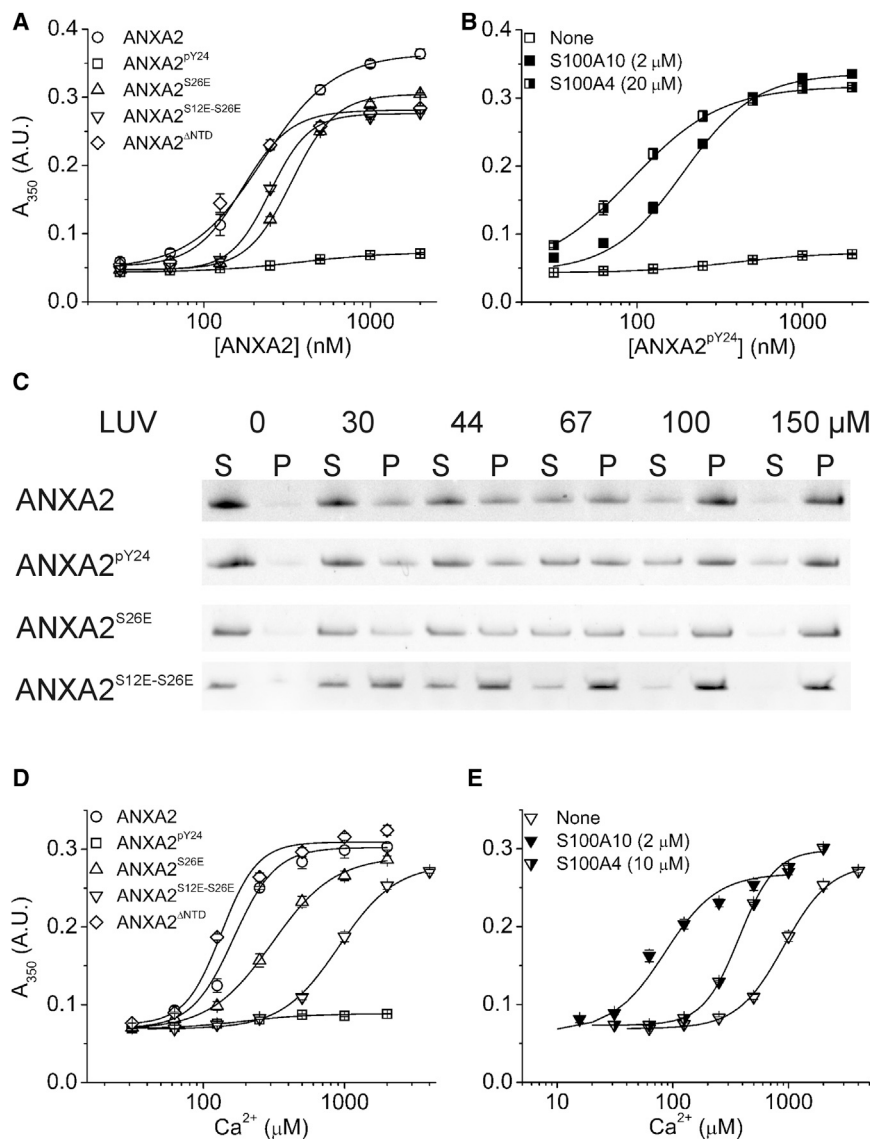


Figure 5. Phosphorylation and S100-Binding Modulates Membrane-Aggregating Properties of ANXA2

(A) LUVs (PC:PS:Chol, 40:20:40) (100 μ M) were titrated with ANXA2 variants. Liposome aggregation was detected by measuring the turbidity of the LUV solution at 350 nm.

(B) LUVs (100 μ M) were titrated with ANXA2^{pY24} in the presence of 2 μ M S100A10 or 20 μ M S100A4 (monomeric S100 concentration). Each data point represents the mean \pm SEM of three independent experiments, and the solid lines show the data fitting to the Hill equation.

(C) Fl-ANXA2 variants (500 nM) were titrated with LUVs. Mixtures were spun down then the supernatants (S) and pellets (P) were separated on Tris-Tricine-SDS gels.

(D) LUVs (100 μ M) were titrated with Ca^{2+} in the presence of 0.5 μ M ANXA2 variants.

(E) The mixture of 0.5 μ M ANXA2^{S12E-S26E} and 100 μ M LUVs were titrated with Ca^{2+} in the absence or in the presence of S100 variants. See Tables S3 and S4 for more information.

(ANXA2^{ANTD}, residues 32–339) through detecting the change in turbidity of LUV solutions (total lipid concentration of 100 μ M). It was found that, in the presence of 2 mM Ca^{2+} , the extent of LUV aggregation induced by wild-type ANXA2, ANXA2^{ANTD}, ANXA2^{S26E}, and ANXA2^{S12E-S26E} was similar, while the amplitude of the turbidity change caused by ANXA2^{pY24} was 11-fold smaller than that caused by native ANXA2 (Figure 5A, Table S3). Then we repeated the titrations in the presence of S100A10 or S100A4 at saturating concentrations of 2 and 20 μ M, respectively. Both S100A10 and S100A4 restored the membrane-bridging activity of ANXA2^{pY24} (Figure 5B) and decreased the half maximal effective concentration (EC_{50}) of the NTD-containing ANXA2 variants from about 300 nM to about 200 and 150 nM, respectively (Table S3). Note that the LUV-bridging properties of ANXA2^{ANTD} were not affected by the presence of S100 proteins (Table S3), and neither Tyr24 phosphorylation nor the Ser-to-Glu mutations affected the LUV-binding capability of ANXA2 (Figure 5C).

We also investigated the effect of S100 binding on the Ca^{2+} dependence of ANXA2-mediated vesicle aggregation, which

is known to be modulated by PKC phosphorylation or phosphomimicking amino acid substitutions (Ayala-Sanmartin et al., 2000; Johnstone et al., 1992). With native ANXA2, the EC_{50} value of Ca^{2+} was about 160 μ M, which increased to 300 and 900 μ M with ANXA2^{S26E} and ANXA2^{S12E-S26E}, respectively (Figure 5D and Table S4). Note that these results are congruent with those previously published by Ayala-Sanmartin and colleagues (Ayala-Sanmartin, 2001; Ayala-Sanmartin et al., 2000). Phosphorylation of Tyr24 and N-terminal deletion did not alter significantly the EC_{50} value of Ca^{2+} (Table S4). Addition of both S100A10 and S100A4 to NTD-containing ANXA2 variants decreased the average EC_{50} of Ca^{2+} from about 400 μ M to 50 and 200 μ M, respectively (Figure 5E (Table S4)). Note that even in the presence of S100A10 the EC_{50} values were in the 10 μ M range, significantly exceeding the previously published values (Ayala-Sanmartin et al., 2000; Drust and Creutz, 1988; Johnstone et al., 1992). This difference might derive from different buffer conditions (pH, salt concentration, type of the reducing agent), as well as from the different source and sequence of the ANXA2 protein. Notwithstanding, we can conclude that, not only the well-characterized ANXA2 binding protein S100A10, but also the Ca^{2+} -dependent S100A4 positively regulates the membrane-aggregating property of ANXA2.

DISCUSSION

Regulation of ANXA2-Mediated Membrane Bridging by Phosphorylation and Pseudo-Phosphorylation

It is well established that protein phosphorylation is the most prevalent post-translational modification that regulates protein

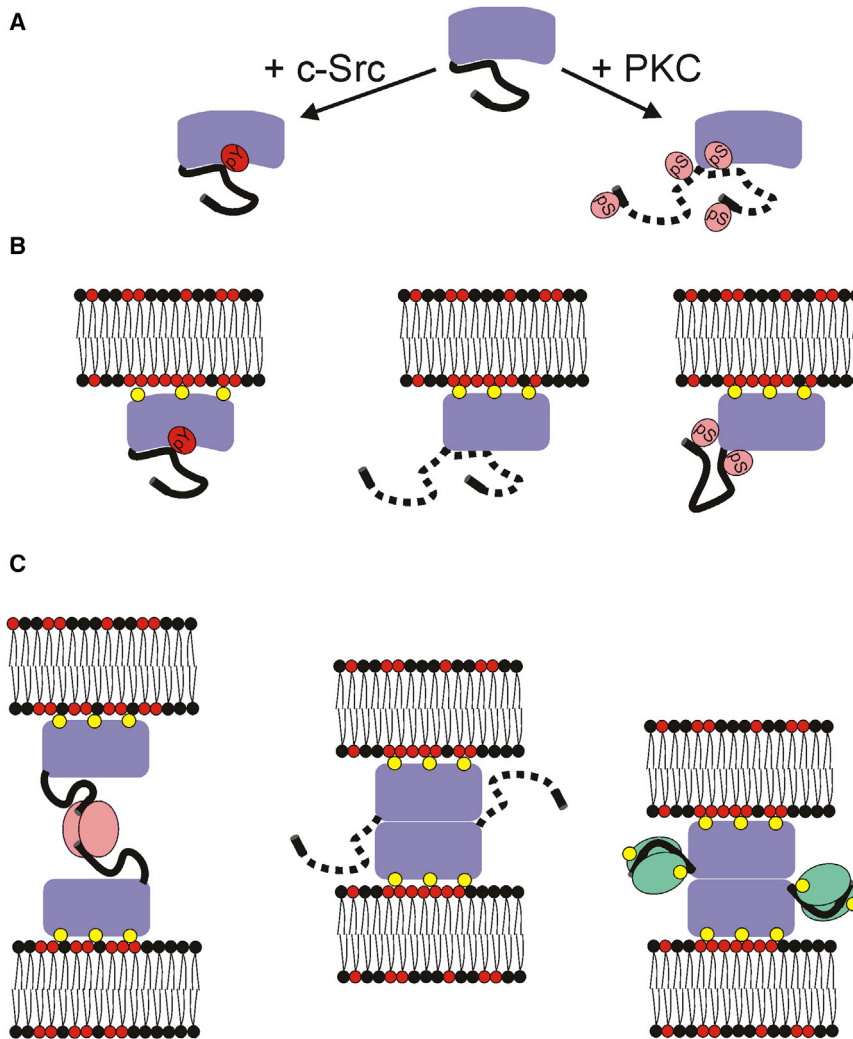


Figure 6. Modulation of ANXA2-Mediated Liposome Aggregation by Protein Phosphorylation and S100 Binding

(A) Conformational flexibility of the NTD increases or decreases as a consequence of Ser26 phosphorylation by PKC (orange) or Tyr24 phosphorylation by c-Src (red), respectively.

(B) Upon Ca^{2+} -dependent (yellow) membrane binding, in contrast to ANXA2^{pY24}, both ANXA2 and ANXA2^{pS12-pS26} adopt an open conformation; however, presumably due to ionic interactions between pSer and Arg side chains in repeat I, ANXA2^{pS12-pS26} is blocked in an “autoinhibited open state.”

(C) Possible models of ANXA2-mediated membrane bridging. The open conformation of native ANXA2 enables self-association leading to the crosslinking of two membranes (middle). S100 proteins restore at least partially the membrane-bridging activity of ANXA2 variants. S100A10 (pink) could promote membrane aggregation through its symmetric interaction with two ANXA2 chains. In turn, S100A4 (green) could act through its asymmetric interaction with the full NTD, which results in the exposition of the concave side of ANXA2 restoring the membrane-bridging activity of ANXA2^{pY24}.

function through conformational modulation (Groban et al., 2006; Volkman et al., 2001). Here we demonstrated that, in ANXA2, the phosphorylation of Tyr24 and the phosphomimetic mutation of Ser26 (also the in silico phosphorylation of Ser26) oppositely regulate the NTD flexibility and the CTD stability. While Tyr24 phosphorylation stabilizes the interaction between the C-NTD and the CTD, shifting the ANXA2 conformational equilibrium toward the “closed” state, the Ser26Glu mutation resulted in the detachment of the C-NTD from the CTD, the conformation of which is referred to here as the “open” state.

These observations, taken together with the results of liposome aggregation assays, point to an ANXA2 regulatory mechanism as depicted in Figure 6. Even though the stability of ANXA2 is more affected by Ca^{2+} binding than by NTD phosphorylation, and the NTD flexibility seems to be interrelated with the CTD stability, the accessibility of the NTD to chymotryptic cleavage, reflecting most directly the open-closed equilibrium, is preferably regulated by C-NTD phosphorylation (Table S1). These data support the view that, in contrast to ANXA1, where Ca^{2+} binding is sufficient to induce an open conformation, the mechanism underlying ANXA2 activation relies on additional regulatory events. Since native ANXA2, which probably adopts a closed

conformation in solution (Figure 6A), aggregates liposomes, such an event could be the membrane binding itself (Figure 6B). Upon membrane binding, ANXA2 is supposed to adopt an open conformation, resembling the Ser26Glu mutant state crystallized herein, which allows the association of ANXA2 molecules through their concave sides (Figure 6C). A conformational change occurring upon membrane binding was suggested by Bellagamba et al. (1997), who demonstrated that the c-Src-mediated Tyr24 phosphorylation is stimulated approximately 6-fold by phosphatidylserine-containing liposomes. We observed that S100A4 bound to ANXA2 variants 6-fold stronger in their LUV-bound form (Table S2), also supporting the theory that ANXA2 adopts an open conformation upon membrane binding. According to previous studies and our results, the phosphomimetic mutation at position 26 moderately affected the LUV-bridging activity of ANXA2; however, when both Ser12 and Ser26 were mutated to Glu (to mimic the hyperphosphorylated form of ANXA2), the effective Ca^{2+} concentration of LUV aggregation increased by almost one order of magnitude (Ayala-Sanmartin et al., 2000). Based on our crystal structure of ANXA2^{S26E} and the MD simulation of ANXA2^{pS26}, we propose a conceivable PKC phosphorylation-dependent inhibitory mechanism as follows. The phosphorylation of Ser26 induces a conformational switch resulting in the dissociation of C-NTD from the CTD and the swapping of the Phe33 side chain to that of Tyr30 in the cavity formed by the annexin repeat I. This latter, along with the ionic interaction of pSer26 with Arg37 and Arg63 (Figure 2A), could explain the negative effect of the single phosphomimetic at

position 26 on the Ca^{2+} sensitivity of vesicle aggregation. Furthermore, this conformational rearrangement and membrane binding could promote the formation of ionic interactions between the pSer12 phosphate group and the guanidine groups of Arg77 and Arg78, leading to a fully “autoinhibited open state” in the hyperphosphorylated ANXA2 (Figure 6B). Alternatively, pSer12 may interact with Arg37 and Arg63, whereas pSer26 may form an ionic bond with Arg304. In any case, these interactions could interfere not only with membrane crosslinking, but also with the binding of S100 proteins. Since the hydration shell of Glu is smaller than that of the phosphorylated Ser and bears only a single negative charge, these ionic interactions should be weaker in ANXA2^{S12E-S26E} than in the PKC-phosphorylated protein, which could explain the lower extent of inhibition induced by the double phosphomimicking substitution than by the effective PKC phosphorylation (Ayala-Sanmartin et al., 2000; Johnstone et al., 1992). To confirm this hypothesis, further high-resolution 3D structural works should be conducted with ANXA2 phosphorylated at positions 12 and 26.

In contrast to the phosphomimicking mutations, Tyr24 phosphorylation almost totally inhibited ANXA2 function. Since we demonstrated that the pTyr24 side chain clamps the C-NTD to the CTD, a possible explanation for the tyrosine phosphorylation-mediated inhibition of LUV aggregation is that the concave side of ANXA2, which is supposedly responsible for ANXA2-ANXA2 interactions during membrane bridging, is masked by the C-NTD in the membrane-bound form as well (Figure 6B).

Although both S100 paralogs restore the LUV-bridging activity of ANXA^{PY24}, the underlying mechanisms are likely different. On the one hand, S100A4 exerts its function through asymmetrically binding the full NTD, which results in the exposure of the concave side of ANXA2, consequently leading to membrane aggregation. On the other hand, the S100A10 dimer binds symmetrically to two ANXA2 chains through the N-terminal part of the NTD, therefore it is able to crosslink the ANXA2-coated membranes regardless of the phosphorylation state of the C-NTD (Figure 6C). Alternatively, S100A10 dimers could bind to two ANXA2 molecules residing at the same membrane surface, followed by membrane crosslinking through the concave side of ANXA2 molecules similar to the S100-unbound or S100A4-bound situation as proposed by others (Menke et al., 2004; Waisman, 1995). The latter model presumes the avid binding of S100A10 to the membrane-bound ANXA2 molecules, consequently, the affinity of membrane-bound ANXA2 to S100A10 should substantially exceed that of the membrane-unbound ANXA2. Since we detected only about a 6-fold increase in affinity, we support the first model, which is also corroborated by the results of cryo-electron microscopic studies carried out at physiological pH in the presence of Ca^{2+} (Illien et al., 2010; Lambert et al., 1997). Although the binding of S100A10 to ANXA2 is not affected by Tyr24 phosphorylation, we suppose that the membrane-bound structure of the heterotetramer is altered through the modulation of the C-NTD-CTD interaction, which could result in the hindered membrane-bridging activity of the heterotetramer at low Ca^{2+} concentration (Hubaishy et al., 1995). Notwithstanding, further studies on membrane-bound ANXA2 structure should be carried out to decipher the detailed mechanism of ANXA2 action involving the interplay of Ca^{2+} , protein phosphorylation, and S100 binding.

Differential Binding of S100A10 and S100A4 to ANXA2

According to our results, S100A4 binds asymmetrically to ANXA2 with a moderate affinity in the micromolar range. Although the asymmetric unit of the crystal structure of ANXA2-S100A4 complex contained two ANXA2 chains, one of which formed a 1:1 interaction with an S100A4 subunit resembling the symmetric structure of the ANXA2-S100A10 complex, the full NTD of the other ANXA2 was wrapped around the S100A4 dimer (Figure 4). Since we demonstrated that S100A4 bound to both free and membrane-bound ANXA2 in an asymmetrical way, we conclude that this S100A10-like interaction is likely a crystallization artifact. Note that Streicher et al. (2009) extensively investigated the interaction of S100 proteins with ANXA1 and ANXA2 N termini, identifying S100A6 and S100A11 as binding partners, also with micromolar affinities. However, they used annexin peptides comprising only the N-terminal 14 residues instead of the full NTD, hence they were unable to detect S100A4 binding to ANXA2. Along similar lines, other ANXA-S100 interactions could remain undiscovered, urging us to conduct binding studies using the full NTD of a given annexin paralog.

To speculate about the possible role of different ANXA2-S100 protein interactions, it is important to keep in mind the following considerations. First, S100A4 activation is Ca^{2+} dependent in contrast to S100A10. Second, although the binding interface of ANXA2 and S100A4 is more extended than that of ANXA2 and S100A10 (1,903 and 968 Å², respectively), the complex formation is much more favorable in the case of S100A10 ($K_d^{\text{S100A10}} = 13 \text{ nM}$ and $K_d^{\text{S100A4}} = 5 \text{ }\mu\text{M}$). Consequently, the ANXA2-S100A4 complex is not formed intracellularly at resting Ca^{2+} concentration, as was proposed for the subnanomolar interaction of S100A4 with NMIIA (Badyal et al., 2011). Moreover, if S100A10 is present, the amount of the ANXA2-S100A4 complex would be negligible. However, in the extracellular milieu, the Ca^{2+} concentration is not limiting, and S100A4 is thought to exert its various physiological and pathological functions, especially in cases where this isoform is overexpressed, for example in several different tumors (Boye and Maelandsmo, 2010; Bresnick et al., 2015). A possible physiological function for the ANXA2-S100 complexes is the regulation of plasmin generation. Plasmin has a key role in extracellular matrix remodeling thus contributes not only to normal cellular differentiation, but also pathological processes such as tumor cell invasion (Lu et al., 2011). Both S100A4 and S100A10 positively regulate ANXA2-mediated plasminogen activation through binding tissue plasminogen activator and plasminogen through their C-terminal lysines (MacLeod et al., 2003; Semov et al., 2005). Moreover, it has been demonstrated that exogenously added S100A4 induced the translocation of ANXA2 to the surface of human primary endothelial cells, which led to enhanced plasminogen activation and capillary-like tube formation (i.e., angiogenesis) (Semov et al., 2005). If we consider that cellular plasmin generation is regulated by a negative feedback mechanism involving the cleavage of the NTD (He et al., 2011; Park et al., 2014), a remarkable functional impact could be assigned to the asymmetric binding of S100A4 to ANXA2. Namely, S100A4, binding the whole NTD, could protect ANXA2 from plasmin-mediated cleavage, resulting in an impaired negative feedback mechanism, which could also contribute to the enhanced metastatic potential of S100A4-expressing cancer cells.

STAR★METHODS

Detailed methods are provided in the online version of this paper and include the following:

- [KEY RESOURCES TABLE](#)
- [CONTACT FOR REAGENT AND RESOURCE SHARING](#)
- [METHOD DETAILS](#)
 - Cloning, Protein Expression and Purification
 - Protein Phosphorylation
 - Fluorescent Labeling
 - LUV Preparation
 - Crystallization, Data Collection and Structure Determination
 - Molecular Dynamic (MD) Simulations
 - Limited Proteolysis (LP)
 - Differential Scanning Fluorimetry (DSF)
 - Fluorescence Polarization (FP) Assays
 - Isothermal Titration Calorimetry (ITC)
 - LUV Binding and Aggregation Assays
- [DATA AND SOFTWARE AVAILABILITY](#)
 - Software
 - Data Resources

ACCESSION NUMBERS

The atomic coordinates have been deposited in the PDB (www.pdb.org) under the following accession numbers (PDB: 5LPU, 5LQ0, 5LQ2, and 5LPX).

SUPPLEMENTAL INFORMATION

Supplemental Information includes one figure and four tables and can be found with this article online at <http://dx.doi.org/10.1016/j.str.2017.06.001>.

AUTHOR CONTRIBUTIONS

E.P., B.K., and G.G. designed research; E.P., B.K., L.R., K.K., I.L., N.J., G.S., and C.H. performed research; E.P., B.K., G.G., G.S., K.L., L.B., B.V., and G.K. analyzed data; and B.K. and L.N. oversaw the research and wrote the paper.

ACKNOWLEDGMENTS

We thank Dr. András Patthy for in-house peptide synthesis, Dr. József Kardos for his expert advice in the analysis of thermal unfolding data, the staff members at the beamlines PXIII of SLS for assistance in data collection, and Dr. Gábor Pál for the careful reading of the manuscript. This work was supported by the National Research, Development and Innovation Office (NKFIH) grants K108437 and K119359 (to L.N.), the MedInProt program of the Hungarian Academy of Sciences (to L.N., B.V., and L.B.), the János Bolyai Research Scholarship of the Hungarian Academy of Sciences (to G.S.), and the National Development Agency grant (KMOP-4.2.1/B-10-2011). Project no. FIEK_16-1-2016-0005 has been implemented with the support provided from the National Research, Development and Innovation Fund of Hungary, financed under the FIEK_16 funding scheme.

Received: February 3, 2017

Revised: April 27, 2017

Accepted: June 1, 2017

Published: June 29, 2017

REFERENCES

Abraham, M.J., Murtola, T., Schulz, R., Páll, S., Smith, J.C., Hess, B., and Lindahl, E. (2015). GROMACS: high performance molecular simulations

through multi-level parallelism from laptops to supercomputers. *SoftwareX* 1, 19–25.

Adams, P.D., Afonine, P.V., Bunkoczi, G., Chen, V.B., Davis, I.W., Echols, N., Headd, J.J., Hung, L.W., Kapral, G.J., Grosse-Kunstleve, R.W., et al. (2010). PHENIX: a comprehensive Python-based system for macromolecular structure solution. *Acta Crystallogr. D Biol. Crystallogr.* 66, 213–221.

Aukrust, I., Evensen, L., Hollas, H., Berven, F., Atkinson, R.A., Trave, G., Flatmark, T., and Vedeler, A. (2006). Engineering, biophysical characterisation and binding properties of a soluble mutant form of annexin A2 domain IV that adopts a partially folded conformation. *J. Mol. Biol.* 363, 469–481.

Ayala-Sanmartin, J. (2001). Cholesterol enhances phospholipid binding and aggregation of annexins by their core domain. *Biochem. Biophys. Res. Commun.* 283, 72–79.

Ayala-Sanmartin, J., Gouache, P., and Henry, J.P. (2000). N-Terminal domain of annexin 2 regulates Ca²⁺-dependent membrane aggregation by the core domain: a site directed mutagenesis study. *Biochemistry* 39, 15190–15198.

Ayala-Sanmartin, J., Henry, J.P., and Pradel, L.A. (2001). Cholesterol regulates membrane binding and aggregation by annexin 2 at submicromolar Ca²⁺ concentration. *Biochim. Biophys. Acta* 1510, 18–28.

Ayala-Sanmartin, J., Zibouche, M., Illien, F., Vincent, M., and Gallay, J. (2008). Insight into the location and dynamics of the annexin A2 N-terminal domain during Ca²⁺-induced membrane bridging. *Biochim. Biophys. Acta* 1778, 472–482.

Badyal, S.K., Basran, J., Bhanji, N., Kim, J.H., Chavda, A.P., Jung, H.S., Craig, R., Elliott, P.R., Irvine, A.F., Barsukov, I.L., et al. (2011). Mechanism of the Ca²⁺-dependent interaction between S100A4 and tail fragments of non-muscle myosin heavy chain IIA. *J. Mol. Biol.* 405, 1004–1026.

Becker, T., Weber, K., and Johnsson, N. (1990). Protein-protein recognition via short amphiphilic helices; a mutational analysis of the binding site of annexin II for p11. *EMBO J.* 9, 4207–4213.

Bellagamba, C., Hubaishy, I., Bjorge, J.D., Fitzpatrick, S.L., Fujita, D.J., and Waisman, D.M. (1997). Tyrosine phosphorylation of annexin II tetramer is stimulated by membrane binding. *J. Biol. Chem.* 272, 3195–3199.

Berendsen, H.J.C., Postma, J.P.M., Vangunsteren, W.F., Dinola, A., and Haak, J.R. (1984). Molecular-dynamics with coupling to an external bath. *J. Chem. Phys.* 81, 3684–3690.

Biri, B., Kiss, B., Kiraly, R., Schlosser, G., Lang, O., Kohidai, L., Fesus, L., and Nyitrai, L. (2016). Metastasis-associated S100A4 is a specific amine donor and an activity-independent binding partner of transglutaminase-2. *Biochem. J.* 473, 31–42.

Boye, K., and Maelandsmo, G.M. (2010). S100A4 and metastasis: a small actor playing many roles. *Am. J. Pathol.* 176, 528–535.

Bresnick, A.R., Weber, D.J., and Zimmer, D.B. (2015). S100 proteins in cancer. *Nat. Rev. Cancer* 15, 96–109.

Buchan, D.W.A., Minneci, F., Nugent, T.C.O., Bryson, K., and Jones, D.T. (2013). Scalable web services for the PSIPRED protein analysis Workbench. *Nucleic Acids Res.* 41, W349–W357.

Bussi, G., Donadio, D., and Parrinello, M. (2007). Canonical sampling through velocity rescaling. *J. Chem. Phys.* 126.

Chasserot-Golaz, S., Vitale, N., Sagot, I., Delouche, B., Dirrig, S., Pradel, L.A., Henry, J.P., Aunis, D., and Bader, M.F. (1996). Annexin II in exocytosis: catecholamine secretion requires the translocation of p36 to the subplasmalemmal region in chromaffin cells. *J. Cell Biol.* 133, 1217–1236.

Cooper, A. (2000). Heat capacity of hydrogen-bonded networks: an alternative view of protein folding thermodynamics. *Biophys. Chem.* 85, 25–39.

Darden, T., York, D., and Pedersen, L. (1993). Particle Mesh Ewald – an N.log(N) method for Ewald sums in large systems. *J. Chem. Phys.* 98, 10089–10092.

Dempsey, B.R., Rezvanpour, A., Lee, T.W., Barber, K.R., Junop, M.S., and Shaw, G.S. (2012). Structure of an asymmetric ternary protein complex provides insight for membrane interaction. *Structure* 20, 1737–1745.

Drucker, P., Pejic, M., Galla, H.J., and Gerke, V. (2013). Lipid segregation and membrane budding induced by the peripheral membrane binding protein annexin A2. *J. Biol. Chem.* 288, 24764–24776.

- Drust, D.S., and Creutz, C.E. (1988). Aggregation of chromaffin granules by calpactin at micromolar levels of calcium. *Nature* 331, 88–91.
- Eden, E.R., Sanchez-Heras, E., Tsapara, A., Sobota, A., Levine, T.P., and Futter, C.E. (2016). Annexin A1 tethers membrane contact sites that mediate ER to endosome cholesterol transport. *Dev. Cell* 37, 473–483.
- Elliott, P.R., Irvine, A.F., Jung, H.S., Tozawa, K., Pastok, M.W., Picone, R., Badyal, S.K., Basran, J., Rudland, P.S., Barraclough, R., et al. (2012). Asymmetric mode of Ca(2+)-S100A4 interaction with nonmuscle myosin IIA generates nanomolar affinity required for filament remodeling. *Structure* 20, 654–666.
- Emsley, P., Lohkamp, B., Scott, W.G., and Cowtan, K. (2010). Features and development of Coot. *Acta Crystallogr. D Biol. Crystallogr.* 66, 486–501.
- Erikson, E., and Erikson, R.L. (1980). Identification of a cellular protein substrate phosphorylated by the avian sarcoma virus-transforming gene product. *Cell* 21, 829–836.
- Fang, Y.T., Lin, C.F., Wang, C.Y., Anderson, R., and Lin, Y.S. (2012). Interferon-gamma stimulates p11-dependent surface expression of annexin A2 in lung epithelial cells to enhance phagocytosis. *J. Cell. Physiol.* 227, 2775–2787.
- Gerke, V., and Moss, S.E. (2002). Annexins: from structure to function. *Physiol. Rev.* 82, 331–371.
- Gerke, V., and Weber, K. (1984). Identity of p36K phosphorylated upon Rous sarcoma virus transformation with a protein purified from brush borders; calcium-dependent binding to non-erythroid spectrin and F-actin. *EMBO J.* 3, 227–233.
- Gingras, A.R., Basran, J., Prescott, A., Kriajevska, M., Bagshaw, C.R., and Barsukov, I.L. (2008). Crystal structure of the Ca(2+)-form and Ca(2+)-binding kinetics of metastasis-associated protein, S100A4. *FEBS Lett.* 582, 1651–1656.
- Glenney, J.R., Jr., and Tack, B.F. (1985). Amino-terminal sequence of p36 and associated p10: identification of the site of tyrosine phosphorylation and homology with S-100. *Proc. Natl. Acad. Sci. USA* 82, 7884–7888.
- Gogl, G., Alexa, A., Kiss, B., Katona, G., Kovacs, M., Bodor, A., Remenyi, A., and Nyitray, L. (2016). Structural basis of ribosomal S6 kinase 1 (RSK1) inhibition by S100B protein: modulation of the extracellular signal-regulated kinase (erk) signaling cascade in a calcium-dependent way. *J. Biol. Chem.* 291, 11–27.
- Gould, K.L., Woodgett, J.R., Isacke, C.M., and Hunter, T. (1986). The protein-tyrosine kinase substrate p36 is also a substrate for protein kinase C in vitro and in vivo. *Mol. Cell. Biol.* 6, 2738–2744.
- Grindheim, A.K., Hollas, H., Ramirez, J., Saraste, J., Trave, G., and Vedeler, A. (2014). Effect of serine phosphorylation and Ser25 phospho-mimicking mutations on nuclear localisation and ligand interactions of annexin A2. *J. Mol. Biol.* 426, 2486–2499.
- Groban, E.S., Narayanan, A., and Jacobson, M.P. (2006). Conformational changes in protein loops and helices induced by post-translational phosphorylation. *PLoS Comput. Biol.* 2, e32.
- He, K.L., Sui, G., Xiong, H., Broekman, M.J., Huang, B., Marcus, A.J., and Hajjar, K.A. (2011). Feedback regulation of endothelial cell surface plasmin generation by PKC-dependent phosphorylation of annexin A2. *J. Biol. Chem.* 286, 15428–15439.
- Hubaishy, I., Jones, P.G., Bjorge, J., Bellagamba, C., Fitzpatrick, S., Fujita, D.J., and Waisman, D.M. (1995). Modulation of annexin II tetramer by tyrosine phosphorylation. *Biochemistry* 34, 14527–14534.
- Illien, F., Finet, S., Lambert, O., and Ayala-Sanmartin, J. (2010). Different molecular arrangements of the tetrameric annexin 2 modulate the size and dynamics of membrane aggregation. *Biochim. Biophys. Acta* 1798, 1790–1796.
- Johnsson, N., Marriott, G., and Weber, K. (1988). p36, the major cytoplasmic substrate of src tyrosine protein kinase, binds to its p11 regulatory subunit via a short amino-terminal amphiphatic helix. *EMBO J.* 7, 2435–2442.
- Johnstone, S.A., Hubaishy, I., and Waisman, D.M. (1992). Phosphorylation of annexin II tetramer by protein kinase C inhibits aggregation of lipid vesicles by the protein. *J. Biol. Chem.* 267, 25976–25981.
- Jorgensen, W.L., Chandrasekhar, J., Madura, J.D., Impey, R.W., and Klein, M.L. (1983). Comparison of simple potential functions for simulating liquid water. *J. Chem. Phys.* 79, 926–935.
- Jost, M., and Gerke, V. (1996). Mapping of a regulatory important site for protein kinase C phosphorylation in the N-terminal domain of annexin II. *Biochim. Biophys. Acta* 1313, 283–289.
- Kabsch, W. (2010). Xds. *Acta Crystallogr. D Biol. Crystallogr.* 66, 125–132.
- Kaetzel, M.A., Mo, Y.D., Mealy, T.R., Campos, B., Bergsma-Schutter, W., Brisson, A., Dedman, J.R., and Seaton, B.A. (2001). Phosphorylation mutants elucidate the mechanism of annexin IV-mediated membrane aggregation. *Biochemistry* 40, 4192–4199.
- Kiss, B., Duelli, A., Radnai, L., Kekesi, K.A., Katona, G., and Nyitray, L. (2012). Crystal structure of the S100A4-nonmuscle myosin IIA tail fragment complex reveals an asymmetric target binding mechanism. *Proc. Natl. Acad. Sci. USA* 109, 6048–6053.
- Lambert, O., Gerke, V., Bader, M.F., Porte, F., and Brisson, A. (1997). Structural analysis of junctions formed between lipid membranes and several annexins by cryo-electron microscopy. *J. Mol. Biol.* 272, 42–55.
- Lee, D.B., Jamgotchian, N., Allen, S.G., Kan, F.W., and Hale, I.L. (2004). Annexin A2 heterotetramer: role in tight junction assembly. *Am. J. Physiol. Renal Physiol.* 287, F481–F491.
- Lindorff-Larsen, K., Piana, S., Palmo, K., Maragakis, P., Klepeis, J.L., Dror, R.O., and Shaw, D.E. (2010). Improved side-chain torsion potentials for the Amber ff99SB protein force field. *Proteins* 78, 1950–1958.
- Liu, L. (1999). Calcium-dependent self-association of annexin II: a possible implication in exocytosis. *Cell. Signal.* 11, 317–324.
- Liu, Y., Myrvang, H.K., and Dekker, L.V. (2015). Annexin A2 complexes with S100 proteins: structure, function and pharmacological manipulation. *Br. J. Pharmacol.* 172, 1664–1676.
- Lizarbe, M.A., Barrasa, J.I., Olmo, N., Gavilanes, F., and Turnay, J. (2013). Annexin-phospholipid interactions. Functional implications. *Int. J. Mol. Sci.* 14, 2652–2683.
- Lu, P., Takai, K., Weaver, V.M., and Werb, Z. (2011). Extracellular matrix degradation and remodeling in development and disease. *Cold Spring Harb. Perspect. Biol.* 3, <http://dx.doi.org/10.1101/cshperspect.a005058>.
- MacLeod, T.J., Kwon, M., Filipenko, N.R., and Waisman, D.M. (2003). Phospholipid-associated annexin A2-S100A10 heterotetramer and its subunits: characterization of the interaction with tissue plasminogen activator, plasminogen, and plasmin. *J. Biol. Chem.* 278, 25577–25584.
- McCoy, A.J. (2007). Solving structures of protein complexes by molecular replacement with Phaser. *Acta Crystallogr. D Biol. Crystallogr.* 63, 32–41.
- Menke, M., Ross, M., Gerke, V., and Steinem, C. (2004). The molecular arrangement of membrane-bound annexin A2-S100A10 tetramer as revealed by scanning force microscopy. *ChemBiochem* 5, 1003–1006.
- Murshudov, G.N., Vagin, A.A., and Dodson, E.J. (1997). Refinement of macromolecular structures by the maximum-likelihood method. *Acta Crystallogr. D Biol. Crystallogr.* 53, 240–255.
- Nose, S., and Klein, M.L. (1983). Constant pressure molecular-dynamics for molecular systems. *Mol. Phys.* 50, 1055–1076.
- Oh, Y.S., Gao, P., Lee, K.W., Ceglia, I., Seo, J.S., Zhang, X., Ahn, J.H., Chait, B.T., Patel, D.J., Kim, Y., et al. (2013). SMARCA3, a chromatin-remodeling factor, is required for p11-dependent antidepressant action. *Cell* 152, 831–843.
- Park, J., Yamaura, T., Kawamoto, J., Kurihara, T., and Sato, S.B. (2014). Reciprocal modulation of surface expression of annexin A2 in a human umbilical vein endothelial cell-derived cell line by eicosapentaenoic acid and docosahexaenoic acid. *PLoS One* 9, e85045.
- Parrinello, M., and Rahman, A. (1981). Polymorphic transitions in single-crystals – a new molecular-dynamics method. *J. Appl. Phys.* 52, 7182–7190.
- Pocsfalvi, G., Cuccurullo, M., Schlosser, G., Scacco, S., Papa, S., and Malorni, A. (2007). Phosphorylation of B14.5a subunit from bovine heart complex I identified by titanium dioxide selective enrichment and shotgun proteomics. *Mol. Cell. Proteomics* 6, 231–237.

- Poeter, M., Radke, S., Koese, M., Hessner, F., Hegemann, A., Musiol, A., Gerke, V., Grewal, T., and Rescher, U. (2013). Disruption of the annexin A1/S100A11 complex increases the migration and clonogenic growth by dysregulating epithelial growth factor (EGF) signaling. *Biochim. Biophys. Acta* 1833, 1700–1711.
- Rety, S., Sopkova, J., Renouard, M., Osterloh, D., Gerke, V., Tabaries, S., Russo-Marie, F., and Lewit-Bentley, A. (1999). The crystal structure of a complex of p11 with the annexin II N-terminal peptide. *Nat. Struct. Biol.* 6, 89–95.
- Rosengarth, A., and Luecke, H. (2003). A calcium-driven conformational switch of the N-terminal and core domains of annexin A1. *J. Mol. Biol.* 326, 1317–1325.
- Rosengarth, A., and Luecke, H. (2004). Annexin A2. Does it induce membrane aggregation by a new multimeric state of the protein? *Annexins 1*, e34–e41.
- Seaton, B.A. (1996). *Annexins: Molecular Structure to Cellular Function* (R.G. Landes).
- Semov, A., Moreno, M.J., Onichtchenko, A., Abulrob, A., Ball, M., Ekiel, I., Pietrzynski, G., Stanimirovic, D., and Alakhov, V. (2005). Metastasis-associated protein S100A4 induces angiogenesis through interaction with annexin II and accelerated plasmin formation. *J. Biol. Chem.* 280, 20833–20841.
- Shih, P., Holland, D.R., and Kirsch, J.F. (1995). Thermal stability determinants of chicken egg-white lysozyme core mutants: hydrophobicity, packing volume, and conserved buried water molecules. *Protein Sci.* 4, 2050–2062.
- Streicher, W.W., Lopez, M.M., and Makhatadze, G.I. (2009). Annexin I and annexin II N-terminal peptides binding to S100 protein family members: specificity and thermodynamic characterization. *Biochemistry* 48, 2788–2798.
- Tran, J.T., Rosengarth, A., and Luecke, H. (2002). Cloning, purification and crystallization of full-length human annexin 2. *Acta Crystallogr. D Biol. Crystallogr.* 58, 1854–1857.
- Tressler, R.J., Updyke, T.V., Yeatman, T., and Nicolson, G.L. (1993). Extracellular annexin II is associated with divalent cation-dependent tumor cell-endothelial cell adhesion of metastatic RAW117 large-cell lymphoma cells. *J. Cell. Biochem.* 53, 265–276.
- van den Berg, S., Lofdahl, P.A., Hard, T., and Berglund, H. (2006). Improved solubility of TEV protease by directed evolution. *J. Biotechnol.* 121, 291–298.
- Vanquielef, E., Simon, S., Marquant, G., Garcia, E., Klimerak, G., Delepine, J.C., Cieplak, P., and Dupradeau, F.Y. (2011). R.E.D. Server: a web service for deriving RESP and ESP charges and building force field libraries for new molecules and molecular fragments. *Nucleic Acids Res.* 39, W511–W517.
- Volkman, B.F., Lipson, D., Wemmer, D.E., and Kern, D. (2001). Two-state allosteric behavior in a single-domain signaling protein. *Science* 291, 2429–2433.
- Waisman, D.M. (1995). Annexin II tetramer: structure and function. *Mol. Cell. Biochem.* 149–150, 301–322.
- Weber, K., Johnsson, N., Plessmann, U., Van, P.N., Soling, H.D., Ampe, C., and Vandekerckhove, J. (1987). The amino acid sequence of protein II and its phosphorylation site for protein kinase C; the domain structure Ca²⁺-modulated lipid binding proteins. *EMBO J.* 6, 1599–1604.
- Xu, X.H., Pan, W., Kang, L.H., Feng, H., and Song, Y.Q. (2015). Association of annexin A2 with cancer development (Review). *Oncol. Rep.* 33, 2121–2128.

STAR★METHODS

KEY RESOURCES TABLE

REAGENT or RESOURCE	SOURCE	IDENTIFIER
Bacterial and Virus Strains		
Bacteria: <i>E.coli</i> DH5 α	NEB	Cat#C29871
Bacteria: <i>E.coli</i> BL21(DE3)	NEB	Cat#C25271
Bacteria: <i>E.coli</i> ArcticExpress	Agilent Technologies	Cat#230192
Chemicals, Peptides, and Recombinant Proteins		
ANXA2 ²⁻¹⁵ peptide	This paper	N/A
ANXA2 ²⁻³³ peptide	This paper	N/A
ANXA2	This paper	UniProt: P07355
ANXA2 ^{pY24}	This paper	N/A
ANXA2 ^{S26E}	This paper	N/A
ANXA2 ^{S12E-S26E}	This paper	N/A
ANXA2 ^{ΔNTD}	This paper	N/A
S100A4	This lab	UniProt: P26447
S100A10	This lab	UniProt: P60903
Tobacco etch virus (TEV) protease	This lab	UniProt: Q0GDU8
EphB1-KD (612-892)	This paper	UniProt: P54762
α -chymotrypsin	Sigma-Aldrich	Cat#C4129
Phosphatidylcholine	Sigma-Aldrich	Cat#P3556
Phosphatidylserine	Sigma-Aldrich	Cat#P7769
Cholesterol	Sigma-Aldrich	Cat#P8667
5-(Iodoacetamido)-fluorescein	Sigma-Aldrich	Cat#I9271
SYPRO Orange dye	Sigma-Aldrich	Cat#S5692
Deposited Data		
Coordinates of ANXA2	Rosengarth and Luecke, 2004	PDB: 1XJL
Coordinates of ANXA2 ^{S26E}	This paper	PDB: 5LPX
Coordinates of ANXA2 ^{pY24}	This paper	PDB: 5LQ0, 5LQ2
Coordinates of ANXA2 – S100A4 complex	This paper	PDB: 5LPU
Oligonucleotides		
ANXA2 ^{S26E} forward: CCAAGTGCATATGGGGAAGTCAAAGCCTATACT'	Sigma-Aldrich	N/A
ANXA2 ^{S26E} reverse: AGTATAGGCTTTGACTTCCCATATGCACTTGG	Sigma-Aldrich	N/A
ANXA2 ^{S12E} forward: CGAAATCCTGTGCAAGCTCGCGTTGGAGGGTGATCAC	Sigma-Aldrich	N/A
ANXA2 ^{S12E} reverse: GTGATCACCTCCAACGCGAGCTTGACAGGATTTG	Sigma-Aldrich	N/A
ANXA2 ^{ΔNTD} forward: cgtaggatccAACTTTGATGCTGAGCGG	Sigma-Aldrich	N/A
ANXA2 ^{ΔNTD} reverse: ctagctcgagtaGTCATCTCCACCACACAG	Sigma-Aldrich	N/A
EphB1-KD forward: tatcatatgAAGGAGATTGATGTATCTTTTGTG	Sigma-Aldrich	N/A
EphB1-KD reverse: tatggatcctaTGCCACAGTCTTGAGACTTG	Sigma-Aldrich	N/A
Recombinant DNA		
ANXA2 in pSE420 vector	Tran et al., 2002	N/A
ANXA2 ^{S26E} in pSE420 vector	This paper	N/A

(Continued on next page)

Continued

REAGENT or RESOURCE	SOURCE	IDENTIFIER
ANXA2 ^{S12E-S26E} in pSE420 vector	This paper	N/A
ANXA2 ^{ΔNTD} in modified pET15b vector (pBH4)	This paper	N/A
EphB1-KD in modified pET15b vector (pEV)	This paper	N/A
S100A10 in modified pET15b vector (pBH4)	Biri et al., 2016	N/A
S100A4 in modified pET15b vector (pBH4)	Kiss et al., 2012	N/A
Tobacco etch virus (TEV) protease in pTH24 vector	van den Berg et al., 2006	N/A
Software and Algorithms		
Coot	Emsley et al., 2010	https://www2.mrc-lmb.cam.ac.uk/personal/
Phenix	Adams et al., 2010	https://www.phenix-online.org
Refmac	Murshudov et al., 1997	http://www.ccp4.ac.uk/html/refmac5.html
Pymol	PYMOL	http://www.pymol.org
Phaser	McCoy, 2007	http://www-structmed.cimr.cam.ac.uk/phaser_obsolete/
XDS	Kabsch, 2010	http://xds.mpimf-heidelberg.mpg.de/
Origin for ITC 5.0	OriginLab	http://www.originlab.com/
PsiRed	Buchan et al., 2013	http://bioinf.cs.ucl.ac.uk/psipred/
R.E.D Server	Vanquelef et al., 2011	http://upjv.q4md-forcefieldtools.org/REDSERVER/
GROMACS 5	Abraham et al., 2015	http://www.gromacs.org/
Amber99sb-ildn force field	Lindorff-Larsen et al., 2010	http://www.gromacs.org/Downloads/User_contributions/Force_fields
GeneTools	GeneTools	http://www.syngene.com/genetools-software-download
TIP3P explicit water molecules	Jorgensen et al., 1983	N/A
Parrinello-Rahman algorithm	Darden et al., 1993	N/A
Velocity rescale algorithm	Bussi et al., 2007	N/A
Berendsen barostat	Berendsen et al., 1984	N/A
Gibbs-Helmholtz equation	Shih et al., 1995	N/A
Other		
Fractogel EMD DEAE 650 (S) anion exchange resin	Merck	Cat#1.16888.0500
Phenyl Sepharose 6 Fast Flow	GE Healthcare	Cat#17-0973-05
HiTrap SP HP cation exchange column	GE Healthcare	Cat#17115101
Jupiter 300 C18 column	Phenomenex	Cat#00A-4053-E0
Avanti Mini-Extruder	Avanti Polar Lipids	Cat#610020
384-well microplates	Corning	Cat#3676
MicroAmp Fast 96-Well Reaction Plate	Life Technologies	Cat#4346906

CONTACT FOR REAGENT AND RESOURCE SHARING

Further information and requests for reagents should be directed to and will be fulfilled by the Lead Contact, László Nyitray (nyitray@elte.hu)

METHOD DETAILS

Cloning, Protein Expression and Purification

Expression vector pSE420, encoding human ANXA2^{A66E} (UniProt accession code: P07355) was a kind gift of Dr. Volker Gerke ([Tran et al., 2002](#)). pSE420-ANXA2^{S26E} and pSE420-ANXA2^{S12E-S26E} constructs were produced using QuikChange mutagenesis. The coding sequence of the deletion mutant ANXA2^{ΔNTD} (residues 32-339) and the protein kinase domain of ephrin type-B receptor 1 (EphB1-KD, residues 612-892, UniProt accession code: P54762) were cloned after a tobacco etch virus (TEV) protease cleavable His₆-tag into the pET15b-derived expression vector pBH4 using BamHI and XhoI sites and pEV using NdeI and BamHI sites, respectively. Human S100A4 and S100A10 (UniProt accession codes: P26447 and P60903, respectively) were cloned as described previously ([Biri et al., 2016](#); [Kiss et al., 2012](#)).

ANXA2 variants and S100 proteins were expressed in *Escherichia coli* BL21(DE3) cells. Transformed cultures were grown in Luria-Bertani (LB) broth supplemented with $100 \mu\text{g} \cdot \text{ml}^{-1}$ at 37°C until the optical density at 600 nm reached 0.6. The protein expression was induced with 0.5 mM isopropyl β -D-1-thiogalactopyranoside (IPTG) at 37°C for 3 h. In the case of ANXA2, ANXA2^{S26E} and ANXA2^{S12E-S26E} the pelleted cells were disintegrated by ultrasonication in a buffer containing 20 mM Tris pH 8, 0.1 mM EDTA, 0.1 mM Tris(2-carboxyethyl)phosphine (TCEP) and 1 mM PMSF. Cell lysate was clarified by centrifugation at $40,000 \times g$, and the supernatant was applied to a Fractogel EMD DEAE 650 (S) anion exchange resin (Merck) equilibrated with lysis buffer. The pH of the flow-through was adjusted with 4-(2-Hydroxyethyl)piperazine-1-ethanesulfonic acid (Hepes) to 6.5, then applied to a HiTrap SP HP cation exchange column (GE Healthcare) to separate ANXA2 variants with a linear gradient of 30–500 mM NaCl in 20 mM Hepes pH 6.5, 0.1 mM TCEP. ANXA2^{ΔNTD} and S100 proteins were purified by Ni²⁺-affinity chromatography using Profinity IMAC resin (Bio-Rad) using 20 mM Tris pH 8, 300 mM NaCl, 0.1 mM TCEP as a lysis and wash buffer. His₆-tagged proteins were eluted with the lysis buffer complemented with 250 mM imidazole. After cleavage of the His₆-tag with TEV protease (van den Berg et al., 2006), ANXA2^{ΔNTD} (carrying an extraneous, cloning related Gly-Ser at the N-terminus) and S100A10 (carrying an extraneous Gly-Ser-His) were separated by cation exchange chromatography using HiTrap SP HP column at pH 6.5 and pH 6, respectively. S100A4 (carrying an extraneous Gly-Ser-His) was applied to Phenyl Sepharose 6 resin (GE Healthcare), washed with 20 mM Hepes, 50 mM NaCl, 0.5 mM CaCl₂, 0.1 mM TCEP, and eluted with the wash buffer supplemented with 5 mM EDTA. The purified proteins were concentrated with Amicon Ultra centrifugation filter units (Merck), equimolar amount of TCEP was added and stored at -70°C .

The catalytically active EphB1-KD was expressed in *Escherichia coli* ArcticExpress cells (Agilent Technologies). The protein expression was induced with 0.1 mM isopropyl β -D-1-thiogalactopyranoside (IPTG) at 12°C for 20 h. The His₆-tagged protein was purified by Ni²⁺-affinity chromatography as described above followed by dialysis against 20 mM Tris, 150 mM NaCl, 0.1 mM TCEP at 4°C . After addition of 10 % glycerol the purified protein was stored at -70°C .

N-terminal ANXA2 fragments ANXA2²⁻¹⁵ (Acetyl-Ser2-Gly15-CONH₂) and ANXA2²⁻³³ (Acetyl-Ser2-Phe33-CONH₂) were synthesized in-house by solid-phase techniques using an ABI 431A peptide synthesizer (Applied Biosystems) and standard N-(9-fluorenyl)-methoxycarbonyl chemistry and separated by reverse-phase HPLC on a Jupiter 300 C18 column (Phenomenex).

Protein Phosphorylation

1 μM EphB1-KD was added to 100 μM ANXA2 in 20 mM Tris pH 7.5, 150 mM NaCl, 10 mM MgCl₂, 200 μM ATP, 1 mM MnCl₂, 0.01 % Triton X-100, 1 mM TCEP buffer. The reaction mixture was incubated overnight at room temperature. After five-fold dilution in 20 mM Hepes pH 6.0, the sample was applied to a HiTrap SP HP cation exchange column and separated with a linear gradient of 30–500 mM NaCl in 20 mM Hepes pH 6.5. Quantitative and selective phosphorylation of Tyr24 was confirmed by mass spectrometry as described previously (Pocsfalvi et al., 2007).

Fluorescent Labeling

ANXA2 protein variants and ANXA2 related peptides were labeled selectively at Cys9 with a 3-fold excess of 5-(Iodoacetamido)-fluorescein (5-IAF, Sigma-Aldrich #I9271) in 20 mM Hepes pH 7.5, 150 mM NaCl, 1 mM TCEP buffer incubating the samples for 3 hours in the dark at room temperature. The fluorescein-conjugated ANXA2 protein variants (referred as FI-ANXA2) were separated from the non-reacted dye by cation exchange chromatography. Labeling efficiency was determined by using molar extinction coefficient $\epsilon_{280} = 33,810 \text{ M}^{-1} \cdot \text{cm}^{-1}$ for ANXA2, and extinction coefficients $\epsilon_{495} = 82,000 \text{ M}^{-1} \cdot \text{cm}^{-1}$ and $\epsilon_{280} = 24,600 \text{ M}^{-1} \cdot \text{cm}^{-1}$ for the fluorescein moiety. Typical degree of labeling was 30–40%. The fluorescein-conjugated peptides were successfully separated from both the non-reacted 5-IAF and the unconjugated peptide by RP-HPLC.

LUV Preparation

Lipid mixture containing 40% phosphatidylcholine (Sigma-Aldrich #P3556), 20% phosphatidylserine (Sigma-Aldrich #P7769) and 40% cholesterol (Sigma-Aldrich #P8667) were prepared in chloroform and then dried using nitrogen gas. Dried lipids were rehydrated to a total lipid concentration of 1 mM in 20 mM Hepes pH 7.5, 150 mM NaCl, 3 mM NaN₃, and 0.1 mM TCEP buffer (Buffer L). After 3 cycles of vortexing and sonication in batch sonicator large unilamellar vesicles (LUVs) were generated by extruding the sample through a polycarbonate membrane of 200 nm pore size using Avanti Mini-Extruder (Avanti Polar Lipids).

Crystallization, Data Collection and Structure Determination

Crystallization samples contained 350 μM ANXA2 variants and 800 μM S100A4 (monomeric concentration) in the case of ANXA2–S100A4 complex in a buffer containing 10 mM CaCl₂ and 5 mM TCEP. Crystallization was done in standard hanging drop vapor-diffusion set-up at 20°C , mixing the protein and the precipitant solutions in an equal volume. Crystals of ANXA2^{Y24} grew in solutions containing 0.1 M MES pH 6.0, 0.1 M MgCl₂, 4% PEG 6000 (structure A) or 0.1 M Tris pH 8.5, 10% ethanol (structure B). ANXA2^{S26E} and the ANXA2–S100A4 complex were crystallized using precipitant solutions consisting of 0.1 M Bis-Tris pH 6.0, 0.2 M ammonium acetate, 5% PEG 3350 and 0.1 M Bis-Tris pH 6.5, 0.2 M ammonium acetate, 4% PEG4000, 1.5% glycerol, respectively. Crystals were supplemented with 20% glycerol before flash cooling in liquid nitrogen. Data were collected on the PXIII beamline of the Swiss Light Source (Villigen) at 100 K with a wavelength of 1 Å (Table 1). Data were processed with XDS (Kabsch, 2010). The phase problem was solved by molecular replacement (MR) in PHASER (McCoy, 2007) with a high resolution structure of S100A4 (Gingras et al., 2008) and ANXA2 (Rosengarth and Luecke, 2004) as searching model. Structure refinement was carried out in PHENIX (Adams et al., 2010) and structure remodeling/building was done in Coot (Emsley et al., 2010) (Table 1). Crystal structures were deposited to the Protein Data

Bank under the accession codes of 5LPU (ANXA2-S100A4), 5LQ0 (ANXA2^{pY24}, structure A), 5LQ2 (ANXA2^{pY24}, structure B) and 5LPX (ANXA2^{S26E}).

Molecular Dynamic (MD) Simulations

The starting MD models were generated using the crystal structure of the Ca²⁺-bound ANXA2 (residues 21-339; PDB ID: 1XJL) supplemented with a disordered N-terminal segment (residues 2-20). Note that in the case of ANXA2^{pS26} the main chain conformation of the C-NTD had to be altered in order to resolve atom clashes caused by in silico phosphorylation of Ser26 (Figure S1). Alternatively, the MD simulation of ANXA2^{pS26} was carried out using the crystal structure of ANXA2^{S26E} (residues 29-339) complemented with residues 2-28 as a disordered N-terminal segment) as initial state. The disordered regions were pre-simulated using specific modifications (i.e. N-terminal acetylation, phosphorylation), then the prefolded states, with their secondary structure predicted on PsiRed (Buchan et al., 2013), were attached to the corresponding ANXA2 “core”. Parameters of modified amino acids were calculated on R.E.D. Server (Vanqualef et al., 2011). Calculations were prepared and done with the GROMACS 5 program package (Abraham et al., 2015). Amber99sb-ildn force field (Lindorff-Larsen et al., 2010) was applied along with neutralizing Na⁺ counter ions and numerous TIP3P explicit water molecules (Jorgensen et al., 1983) filling a 10 Å spacing between the protein parts and the edges of the dodecahedral simulation box. MD simulations were preceded by two-step minimization process and equilibration. In the first step a steepest descent (sd) optimization was done, with the convergence threshold set to 10³ kJ · mol⁻¹ · nm⁻¹. It was followed by a conjugate gradient (cg) calculation with convergence threshold changed to 10 kJ · mol⁻¹ · nm⁻¹. The optimized system was equilibrated under NPT conditions for 10 ns. Position restraints were applied on solute heavy atoms with a force constant of 10³ kJ · mol⁻¹ · nm⁻² in all optimization and equilibration steps. The lengths of productive simulations were 300 ns, with a time step of 2 fs. ANXA2-bound calcium ions were restrained according to the crystal structures in all steps. Pressure was coupled with the Berendsen barostat (Berendsen et al., 1984) during equilibration and with the Parrinello-Rahman algorithm (Darden et al., 1993; Nose and Klein, 1983; Parrinello and Rahman, 1981) during production, with coupling time constant of 0.5 ps, compressibility of 4.5 · 10⁻⁵ bar⁻¹ and reference pressure of 1 bar. The velocity rescale algorithm (Bussi et al., 2007) was applied for temperature coupling, solute and solvent were coupled separately with a coupling time constant of 0.1 ps to 300 K. Particle Mesh-Ewald summation was used for long range electrostatics. Van der Waals and Coulomb interactions had a cut-off at 11 Å.

Limited Proteolysis (LP)

500 nM FI-ANXA2 variants were mixed with 50 nM α -chymotrypsin (Sigma-Aldrich # C4129) in 330 μ l Buffer L or in Buffer C (Buffer L complemented with 2 mM CaCl₂) in duplicates. The 30 μ l samples, which were taken at different time intervals, were pipetted to the 20 μ l of 1:1 mixture of 5 \times SDS sample buffer and 1 M HCl to ensure that the protease is inactivated immediately. 10 μ l of each sample was separated on 10% Tris-Tricine-SDS gel. The gels were digitalized with Gene Genius Bio Imaging System (Syngene) using Dark Reader transilluminator (Clare) as a light source combined with an amber screen. Densitometric analysis was performed by GeneTools software. Normalized density data were plotted against time and fitted to a single exponential function.

Differential Scanning Fluorimetry (DSF)

DSF experiments were carried out with StepOnePlus Real Time PCR System (Thermo Scientific) using MicroAmp Fast 96-Well Reaction Plate (Life Technologies). Prior to the experiment 10 μ M ANXA2 variants were mixed with the 1:1,000 diluted SYPRO Orange dye (Sigma-Aldrich) in a ratio of 1:1 in Buffer L or in Buffer C. Measurements were performed in a reaction volume of 20 μ l in triplicate. The temperature ramp was 1°C · min⁻¹ over a temperature range of 25-80 °C. The fluorescence intensity was detected at every 1 °C interval. Melting curves were fitted according to the Gibbs-Helmholtz equation (Shih et al., 1995). ΔC_p of unfolding was set to 15 kJ · K⁻¹ · mol⁻¹ in accordance with Cooper who estimated that the contribution of a residue to ΔC_p is approximately 0.05 kJ · K⁻¹ · mol⁻¹ in a globular protein (Cooper, 2000).

Fluorescence Polarization (FP) Assays

FP measurements were carried out using 50 nM FI-ANXA2 fragments and variants (with or without 50 μ M LUV) in Buffer C. The change in FP values upon addition of S100 proteins was measured in 384-well microplates (Corning #3676) in triplicate using Synergy H4 multi-mode microplate reader. Data analysis was performed using the quadratic binding equation in direct titration experiments or a competitive binding equation in competitive binding studies.

Isothermal Titration Calorimetry (ITC)

Titration were carried out at 25 °C in 20 mM Hepes pH 7.5, 150 mM NaCl, 1 mM CaCl₂ and 1 mM TCEP using a Microcal VP-ITC apparatus. The first 2.5 μ l injection was followed by 7.5 μ l injections with a 400-second time interval between each injection. The Origin for ITC 5.0 (OriginLab) software package was used for data processing and the model “One Set of Sites” was fitted.

LUV Binding and Aggregation Assays

LUV-binding of FI-ANXA2 variants was investigated by liposome co-sedimentation assay. 500 nM FI-ANXA2 was incubated for 15 min at room temperature in Buffer C in the presence of increasing amount of LUV (total lipid concentration: 0-150 μ M) in duplicates. Liposomes were spun down by centrifugation at 30,000 \times g for 30 min. The supernatants were removed and mixed with 20 μ l 4 \times SDS sample buffer. Then the pellets were resuspended in 70 μ l 1 \times sample buffer. 10 μ l of each sample was separated on 10%

Tris-Tricine-SDS gel. The gels were digitalized as described above. LUV aggregation was detected by measuring the turbidity of 100 μ M LUV solutions at 350 nm with a path length of 1 cm. Titrations of LUVs with ANXA2 variants were done in triplicate. The experimental data were fitted to the Hill equation.

DATA AND SOFTWARE AVAILABILITY

Software

Software used in this study has been previously published as detailed in the [Key Resources Table](#)

Data Resources

Coordinates and structure factors have been deposited in the Protein Data Bank under accession codes 5LPU, 5LQ0, 5LQ2 and 5LPX.